Biomaterials 289 (2022) 121757

Contents lists available at ScienceDirect

Biomaterials

journal homepage: www.elsevier.com/locate/biomaterials

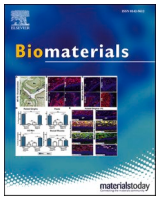

Ru(II)-modified TiO_2 nanoparticles for hypoxia-adaptive photo-immunotherapy of oral squamous cell carcinoma

Jia-Ying Zhou [a,b,1], Wen-Jin Wang [c,1], Chen-Yu Zhang [a,b,1], Yu-Yi Ling [c,1], Xiao-Jing Hong [a,b], Qiao Su [d], Wu-Guo Li [d], Zong-Wan Mao [c,****], Bin Cheng [a,b,***], Cai-Ping Tan [c,**], Tong Wu [a,b,*]

[a] Hospital of Stomatology, Guanghua School of Stomatology, Sun Yat-sen University, Guangzhou, 510055, PR China
[b] Guangdong Provincial Key Laboratory of Stomatology, Guangzhou, 510080, PR China
[c] MOE Key Laboratory of Bioinorganic and Synthetic Chemistry, School of Chemistry, Sun Yat-sen University, Guangzhou, 510006, PR China
[d] Animal Experiment Center, The First Affiliated Hospital, Sun Yat-sen University, Guangzhou, 510080, PR China

ARTICLE INFO

Keywords:
Titanium dioxide
Ruthenium
Photo-immunotherapy
Oral squamous cell carcinoma
Hypoxia adaptation

ABSTRACT

The alternations in the hypoxic and immune microenvironment are closely related to the therapeutic effect and prognosis of oral squamous cell carcinoma (OSCC). Herein, a new nanocomposite, **TiO_2@Ru@siRNA** is constructed from a ruthenium-based photosensitizer (**Ru**) modified-**TiO_2** nanoparticles (NPs) loaded with siRNA of hypoxia-inducible factor-1α (HIF-1α). Under visible light irradiation, **TiO_2@Ru@siRNA** can elicit both Type I and Type II photodynamic effects, which causes lysosomal damage, HIF-1α gene silencing, and OSCC cell elimination efficiently. As a consequence of hypoxia relief and pyroptosis induction, **TiO_2@Ru@siRNA** reshapes the immune microenvironment by downregulation of key immunosuppressive factors, upregulation of immune cytokines, and activation of $CD4^+$ and $CD8^+$ T lymphocytes. Furthermore, patient-derived xenograft (PDX) and rat oral experimental carcinogenesis models prove that **TiO_2@Ru@siRNA**-mediated photodynamic therapy significantly inhibits the tumor growth and progression, and markedly enhances cancer immunity. In all, this study presents an effective hypoxia-adaptive photo-immunotherapeutic nanosystem with great potential for OSCC prevention and treatment.

1. Introduction

Surgical resection remains the primary therapy at present for oral squamous cell carcinoma (OSCC), with chemotherapy and radiotherapy as the main adjuvant treatments [1]. However, the 5-year overall survival rate still remains 60% with such multimodality treatments, which cause significant mutilation leading to life quality reduction simultaneously [2]. Photodynamic therapy (PDT), an effective therapeutic modality in spatiotemporal selectivity superficial tumor, which is based on photosensitizers (PSs) constructed with nanomaterials, has become popular for OSCC prevention and treatment [3,4]. Because of its advantages such as higher specificity and repeatability, lower drug resistance and fewer side effects, PDT has become a promising technique as a primary cancer prevention and treatment modality for OSCC patients with early stages of the disease [5,6].

Hypoxia is a common phenomenon in solid tumors, and OSCC is characterized by large areas of tumoral necrosis and local hypoxia, which causes low response to chemotherapy or even drug resistance [7]. Immunosuppression is another factor accounting for the low-response therapy and poor prognosis of OSCC [8]. Bioinformatics analysis shows that the expression of hypoxia-inducible factor-1α (HIF-1α) and programmed death ligand-1 (PD-L1) is significantly more abundant in OSCC patients with poor prognosis ($p < 0.05$) in public database (Figure S1). Moreover, HIF-1α can upregulate the expression of PD-L1 in glioma, endometrial carcinoma and lung cancer [9–11]. Thus hypoxia adaption combined with PD-L1 blockage may be one of the most

* Corresponding authors. Hospital of Stomatology, Guanghua School of Stomatology, Sun Yat-sen University, Guangzhou, 510055, PR China.
** Corresponding author.
*** Corresponding author.
**** Corresponding author.
E-mail addresses: cesmzw@mail.sysu.edu.cn (Z.-W. Mao), chengbin@mail.sysu.edu.cn (B. Cheng), tancaip@mail.sysu.edu.cn (C.-P. Tan), wutong23@mail.sysu.edu.cn (T. Wu).
[1] These authors contributed equally to this work.

https://doi.org/10.1016/j.biomaterials.2022.121757
Received 15 June 2022; Received in revised form 2 August 2022; Accepted 18 August 2022
Available online 24 August 2022

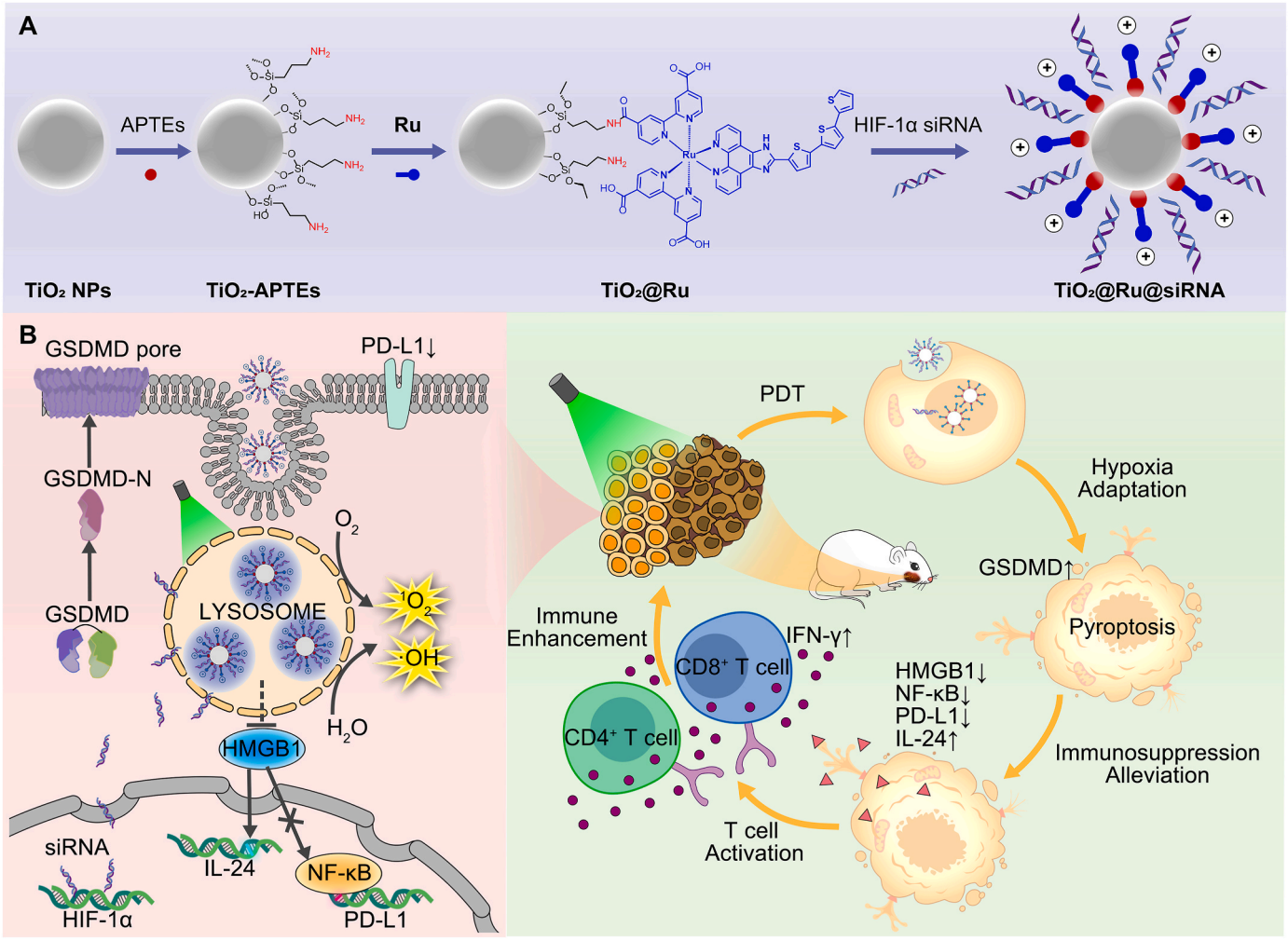

Scheme 1. (A) Construction of the nanocomposite **TiO_2@Ru@siRNA**. (B) Action mechanism of **TiO_2@Ru@siRNA**. ROS: Reactive oxygen species; HIF-1α: Hypoxia-inducible factor-1α; HMGB1: High mobility group box-1 protein; NF-κB: Nuclear factor-kappa B; PD-L1: Programmed death ligand-1; IL-24: Interleukin-24; GSDMD: Gasdermin D; PDT: Photodynamic therapy; IFN-γ: Interferon-gamma.

promising approaches to activate antitumor immunity.

Since most of PDT treatments are based on the production of singlet oxygen ($^1O_2$), one of the biggest challenges of PDT is modulating the hypoxic microenvironment [12–14]. Several strategies have been developed to combat tumor hypoxia, including transporting or generation of oxygen at tumor sites, such as hyperbaric oxygen, oxygen transportation by nanocapsules or perfluorocarbon, dissociation of oxygen from oxyhemoglobin, H_2O_2 degradation, water decomposition and reduction of oxygen consumption [15–19]. Developing PSs through O_2-independent mechanism is another feasible strategy to overcome tumor hypoxia [20–24]. Especially, an oxygen independent PS TOOKAD®-Soluble (a derivative of the photosynthetic pigment bacteriochlorophyll α with palladium as metal center), which mainly produces superoxide anion ($\bullet O_2^-$) or hydroxyl radical (•OH), has been clinically approved in several countries [25–27].

Metal polypyridyl complexes have attracted more and more attention as potent PSs, among which a Ru(II) complex TLD-1433, has entered phase II clinical trial for non-muscle-invasive bladder cancer in Canada [28,29]. The construction of TLD-1433 utilizes the high efficiency of the intersystem crossing process of the Ru(II) center to obtain a populated long-lived excited triplet intraligand charge transfer state, which can generate $^1O_2$ in high quantum yields or interact with the biological environments by electron transfer reactions [28,29]. Interestingly, TLD-1433 has phototoxic effects under hypoxia, and it can cause DNA damage in the absence of oxygen, indicating that it may have other potential mechanisms [25,28].

Titanium dioxide (**TiO_2**) is one of the most widely used nanomaterials in human life, and **TiO_2**-based materials have also been widely investigated as PSs in PDT since the discovery of its photocatalytic activity in 1972 [30–32]. Under radiation, **TiO_2** can usually damage cells by reacting with water to produce reactive oxygen species (ROS). Due to its excellent biocompatibility, **TiO_2** is also used as a drug delivery system for prosthesis implantation and early diseases treatment including cancer [31,32]. Unfortunately, the light response range of **TiO_2** is limited to the ultraviolet region with poor permeability [33]. Different modifications are used to extend the absorption wavelength of **TiO_2** even to the near-infrared range [34–37]. The transfer of photo-electrons from the modifiers (antennas or nanocomposites) to the conduction band (CB) of **TiO_2** can achieve efficient electron hole separation, which is conducive to the reaction between electrons and O_2 to produce $^1O_2$, while the reaction between holes and water molecules can produce •OH and a variety of reactive oxygen radicals [34–37]. These properties make modified **TiO_2** nanoparticles (NPs) ideal biocompatible PSs that can exert PDT effects in both O_2-dependent and -independent manners.

Herein, we constructed a hypoxia-adaptive nanocomposite **TiO_2@Ru@siRNA** for prevention and treatment of OSCC. **TiO_2@Ru@siRNA** is constructed by coupling a **Ru** complex with a similar structure as TLD1433 to **TiO_2** NPs, and a siRNA targeting HIF-1α is further loaded (Scheme 1). **TiO_2@Ru@siRNA** can produce ROS through both type I and type II PDT under visible light (525 nm) irradiation. With

a photocytotoxicity index (PI) up to more than 2000, **TiO_2@Ru@siRNA**-mediated PDT causes lysosomal damage to effectively promote siRNA escape and induce pyroptosis of OSCC cells, which activates multifaceted cancer immune responses. In particular, the PDT effects of **TiO_2@Ru@siRNA** are confirmed in patient-derived xenograft (PDX) model and 4-nitroquinoline-1-oxide (4NQO) induced rat oral carcinogenesis model. Collectively, **TiO_2@Ru@siRNA** has outstanding PDT performance and immunomodulatory function for OSCC through hypoxia adaptation and cancer immune microenvironment optimization. The possibility of potential clinical transformation of this system is still under exploration.

2. Materials and methods

2.1. Materials

All reagents were commercially available and used without further purification. $RuCl_3 \bullet 3H_2O$ was obtained from Adams Chemical, China. Dimethyl [2,2′-bipyridine]-4,4′-dicarboxylate (dimbpc) and aminopropyltriethoxysilane (APTEs) were purchased from Bidepharm (China). 5-formyl-2,2′:5′,2″-terthiophene and 1,10-Phenanthroline-5,6-dione were bought from Energy Chemical (China). Methyl Thiazol Tetrazolium (MTT) was purchased from J&K Chemical (China). Reactive Oxygen Species Assay Kit (2′,7′-dichlorodihydrofluorescein diacetate, DCFH-DA), 4% Paraformaldehyde Fix Solution (4% PFA fix solution), RIPA-Lysis Buffer, SDS-PAGE Sample Loading Buffer, hematoxylin and eosin were obtained from Beyotime Biotechnology (China). RNeasy Minikit was bought from Qiagen (Germany). PrimeScript RT Master Mix was bought from TaKaRa (China). SYBR Green Master Mix was bought from Yeasen (China). 2-Phenyl-1,2-benzisoselenazol-3(2H)-one (Ebselen) was purchased from MedChemExpress (China). 4,5-Dihydroxy-1,3-benzenedisulfonic acid disodium salt monohydrate (Tiron), Sodium pyruvate (NaP), D-mannitol, phosphate buffered saline (PBS), dimethyl sulfoxide (DMSO), phorbol 12-myristate 13-acetate (PMA), ionomycin and 4-nitroquinoline-1-oxide (4NQO) were purchased from Sigma-Aldrich (USA). Fetal bovine serum (FBS), trypsin, Dulbecco's modified Eagle's medium (DMEM), Roswell Park Memorial Institute Medium (RPMI1640 Medium), streptomycin, and LysoTracker Deep Red (LTDR) were purchased from Gibco (Thermo Fisher Scientific, USA). FITC anti-human CD4, Brilliant Violet 605 anti-human CD8, BV421 anti-human IFN-γ, Brefeldin A (BFA), Human TruStain FcX (Fc Receptor Blocking Solution), Fixation Buffer, Intracellular Staining Permeabilization Wash Buffer, and Permeabilization Wash Buffer were purchased from BioLegend (USA). Alexa Fluor® 488 Rabbit monoclonal to HMGB1, Alexa Fluor® 647 Rabbit monoclonal to Calreticulin (CRT), anti–HIF–1 alpha antibody, anti-GSDMD antibody, anti-Cleaved Caspase-1 antibody, anti-β-Actin antibody, anti–NF–κB p65 antibody, anti-PD-L1 antibody, anti-Ki67 antibody, and anti-CD3 antibody were purchased from Abcam (UK) and used as recommended by the manufacturer.

2.2. Instruments

ESI-MS was carried out on a Thermo Scientific LTQ linear ion trap mass spectrometer. ^{1}H NMR and ^{13}C NMR were recorded by a Bruker Advance III 400 MHz spectrometer (Germany). Chemical shifts were referenced relative to the internal solvent signals. The UV–Vis absorption spectra were obtained on a Varian Cary 100 spectrophotometer (Agilent technologies, USA). Microanalyses (C, H, and N) were carried out using an Elemental Vario EL CHNS analyzer (Germany). The fluorescence emission spectra were obtained on an FLS 980 combined fluorescence lifetime and steady state spectrometer (Edinburgh Instrument, UK). The Zeta potentials and hydrodynamic diameters of **TiO_2-APTEs**, **TiO_2@Ru** and **TiO_2@Ru@siRNA** samples dissolved in deionized water were measured by EliteSizer (Brookhaven Instruments; USA) at 25 °C. Morphology of the nanoparticles was analyzed using a Transmission Electron Microscopy (TEM, T12, FEI Tecnai G2 Spirit, Holland). Cell imaging experiments were carried out on a confocal microscope (Zeiss LSM-710, ZEISS, Germany). Cell viability assay was determined using a microplate spectrophotometer (Infinite M200 Pro, Tecan, Switzerland). Flow cytometry was performed on a LSRFortessa (BD Biosciences, USA) and Cytoflex flow cytometer (Becton Dickinson, USA).

2.3. Synthesis

cis-[$RuCl_2(DMSO)_4$], and TTIP (2-([2,2':5′,2″-terthiophen]-5-yl)-1H-imidazo[4,5-f][1,10]phenanthroline) were synthesized by literature methods [38,39].

[$Ru(dimbpc)_2Cl_2$]: dimbpc (1.36 g, 5.00 mmol) and *cis*-[$RuCl_2(DMSO)_4$] (1.21 g, 2.50 mmol) were dispersed in N,N-dimethylformamide (DMF; 20 mL). Then, the reaction mixture was refluxed for 6 h. Then, after evaporation of DMF, 50 mL pre-cold acetone was added. The solution was stored at 0 °C for 2 h. And the solid was filtered and washed with acetone and water until the filtrate became colorless. [$Ru(dimbpc)_2Cl_2$] was obtained as a black solid. Yield: 1.17 g (63.9%).

[$Ru(dimbpc)_2(TTIP)](Cl)_2$ (Rua): [$Ru(dimbpc)_2Cl_2$] (723.53 mg, 1.00 mmol) and TTIP (446.60 mg, 1.00 mmol) were dispersed in 4 mL MeOH. The reaction was rapidly heated to 150 °C in a microwave reactor and maintained for 10 min. Then, the reaction was filtered. The liquid phase was collected and purified through flash chromatography on a silica column ($MeCN/H_2O$/20%KCl, v/v/v = 90/10/1). Evaporation of the solvent under nitrogen afforded the product as a red solid. Yield: 479.4 mg (43.1%). ^{1}H NMR (400 MHz, DMSO-d_6) δ (ppm) 14.60 (s, 1H), 9.41 (d, J = 7.2 Hz, 4H), 9.04 (d, J = 6.1 Hz, 2H), 8.13–8.06 (m, 4H), 7.96 (d, J = 3.6 Hz, 2H),7.90 (dd, J = 5.6 Hz and 1.2 Hz, 2H), 7.85 (d, J = 6.0 Hz, 2H), 7.75 (d, J = 7.2 Hz, 1H), 7.58 (d, J = 12.0 Hz, 1H), 7.54 (d, J = 8.0 Hz, 1H), 7.46 (d, J = 2.8 Hz, 1H) 7.40 (dd, J = 3.8, 0.7 Hz, 1H), 7.35 (d, J = 2.8 Hz, 1H), 7.14 (dd, J = 3.8 and 2.8 Hz, 1H), 4.01 (s, 6H), 3.94 (s, 6H). ^{13}C NMR (400 MHz, DMSO-d_6) δ (ppm) 163.90, 163.81, 157.27, 157.00, 152.95, 152.56, 147.60, 138.63, 138.11, 137.99, 136.48, 135.60, 134.12, 130.77, 128.46, 126.64, 126.17, 126.08, 125.12, 124.61, 123.87, 53.29, 53.23. ESI-MS m/z (CH_3OH): calculated for $[M-2(Cl)]^{2+}$ ($C_{53}H_{38}N_8O_8RuS_3^{2+}$) 556.05, found 556.44; calculated for $[M-2(Cl)-H]^+$ ($C_{53}H_{37}N_8O_8RuS_3^{2+}$) 1111.09, found 1111.46.

[$Ru(bpc)_2(TTIP)](Cl_2)$ (Ru) (bpc = [2,2′-bipyridine]-4,4′-dicarboxylic acid): [$Ru(dimbpc)_2(TTIP)](Cl)_2$ (118.3 mg, 0.1 mmol) was dispersed in a 1 N NaOH solution, and refluxed for 1 h. After then, the reaction was cooled to 0 °C and acidized with 1 N HCl to cat. pH 3 was to obtain the precipitation of **Ru**. The precipitation was filtered and washed with 10 mL MeOH. Then, the solid was dissolved using 1 N NaOH to remove insoluble composition. The liquid phase was acidized and afforded the precipitation of **Ru**. The precipitation was filtered and washed with MeOH and water, and then dried in vacuo to obtain the **Ru** as a dark red solid. Yield: 107.9 mg (91.2%). ^{1}H NMR (400 MHz, MeOD) δ 9.13 (dd, J = 8.3, 1.0 Hz, 2H), 9.11–9.03 (m, 4H), 8.00 (d, J = 5.8 Hz, 2H), 7.91–7.85 (m, 4H), 7.81 (d, J = 3.8 Hz, 1H), 7.74–7.63 (m, 6H), 7.33 (dd, J = 5.1, 0.9 Hz, 1H), 7.30–7.20 (m, 3H), 7.16 (d, J = 3.8 Hz, 1H), 7.05 (dd, J = 5.1, 3.7 Hz, 1H). ^{13}C NMR (101 MHz, MeOD) δ 170.19, 159.01, 158.82, 158.72, 152.87, 152.49, 148.71, 148.59, 148.41, 145.56, 140.07, 139.79, 138.23, 137.78, 137.60, 137.35, 131.75, 129.07, 127.91, 127.74, 127.43, 126.66, 126.07, 125.73, 125.54, 125.28, 124.83, 124.66, 124.61. ESI-MS m/z (CH_3OH): calculated for $[M-2(Cl)]^{2+}$ ($C_{49}H_{30}N_8O_8RuS_3^{2+}$) 528.02, found 528.35; calculated for $[M-2(Cl)-H]^+$ ($C_{49}H_{29}N_8O_8RuS_3^{2+}$) 1055.03, found 1055.13.

TiO_2-APTEs: Using reported amino silanization method [40], the **TiO_2** nanoparticles were modified with an activated silane coupling agent APTEs to obtain positively charged **TiO_2-APTEs**. In brief, the **TiO_2** suspension was prepared by adding 2.1 mg **TiO_2** nanoparticles to 7 mL of methanol solution, followed by an ultrasonic dispersion for 15 min. A reaction liquid was prepared by adding 1 mL APTEs to 14 mL methanol

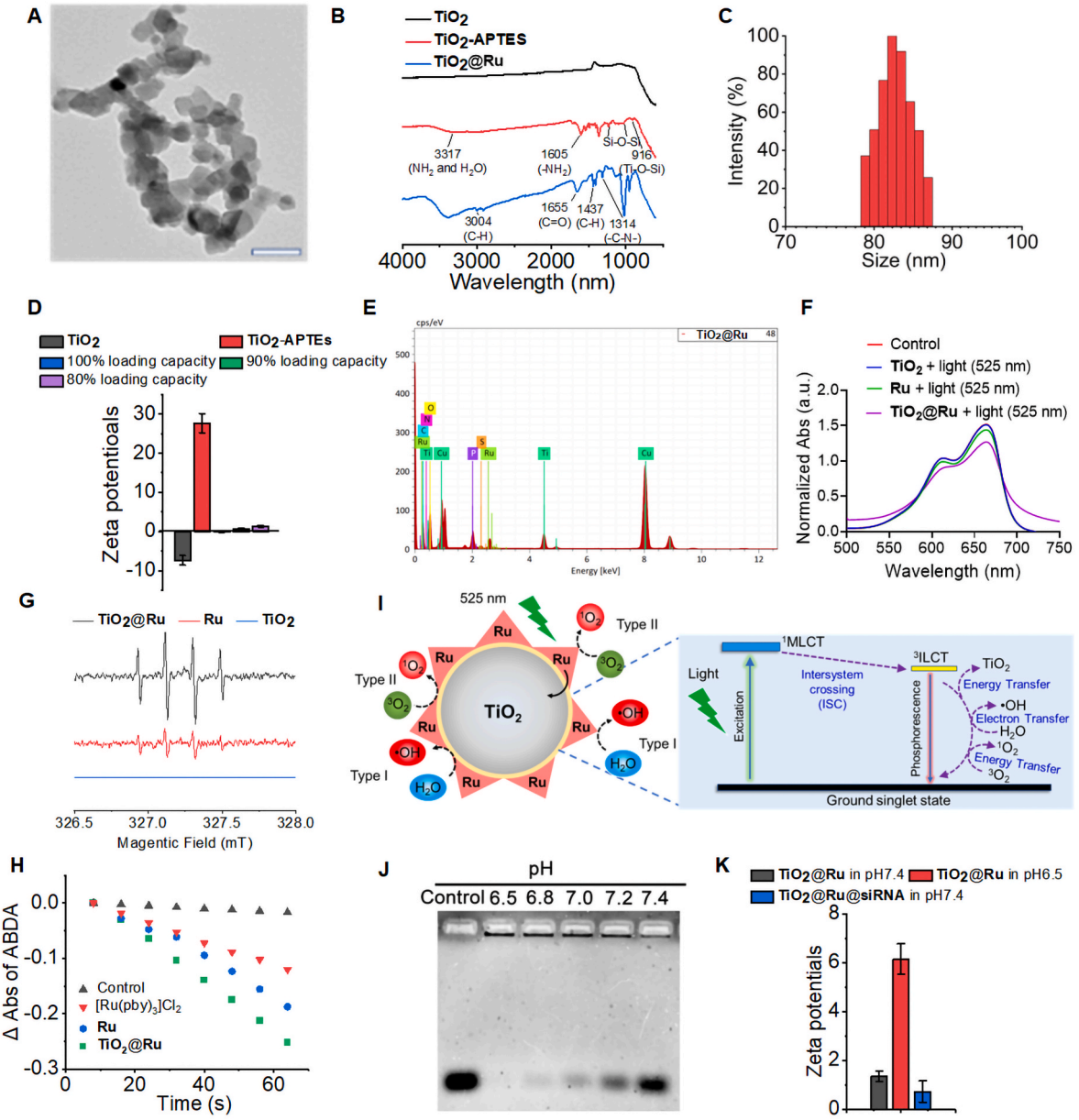

Fig. 1. Characterization of the **TiO_2@Ru** NPs. (A) TEM image of the **TiO_2@Ru** NPs. Scale bar: 100 nm. (B) IR absorption spectra of **TiO_2**, **TiO_2-APTEs** and **TiO_2@Ru**. (C) Hydrodynamic diameter of the **TiO_2@Ru** nanoparticles and their distribution measured by DLS. (D) Zeta potentials of the **TiO_2**, **TiO_2-APTEs** and **TiO_2@Ru** NPs with different loading ratios. (E) Quantitative EDX analysis of **TiO_2@Ru**. (F) The photocatalytic water splitting mechanism on **TiO_2@Ru** under visible light irradiation (525 nm, 15 mW cm^{-2}, 30 min). The decay curves of MB absorption at 660 nm **TiO_2@Ru**: 2 μg/mL; MB: 100 μM. (G) The ESR spectra of •OH generated by **TiO_2@Ru, Ru** and **TiO_2** after light irradiation (525 nm, 15 mW cm^{-2}, 30 min) using DMPO as the •OH trap. **TiO_2@Ru**: 2 μg/mL; DMPO: 100 μM. (H) The degradation rate of ABDA photosensitized by **TiO_2@Ru, Ru** and $[Ru(bpy)_3]Cl_2$ in aerated PBS as shown by the decrease in the absorption maxima of ABDA at 380 nm **TiO_2@Ru**: 2 μg/mL; ABDA: 100 μM. (I) The mechanisms of **TiO_2@Ru** NPs to generate ROS through both Type I and Type II pathways. (J) Agarose gel electrophoresis of free siRNA (2 μM) and **TiO_2@Ru** complex (200 μg/mL) mixed at different pH. (K) Zeta potentials of the **TiO_2@Ru** before and after loading of HIF-1α siRNA.

solution, after which 0.7 mL ammonia solution was also added to the combination that had been stirred for 15 min. Then the **TiO_2** suspension was added in drops into the reaction liquid with vigorous stirring, and the mixture was then stirred for 24 h at room temperature to form **TiO_2-APTEs**.

TiO_2@Ru: **Ru** (16.9 mg, 0.015 mmol) and 2-(7-Azabenzotriazol-1-yl)-N,N,N′,N′-tetramethyluronium hexafluorophosphate (11.4 mg, 0.03 mmol) were dissolved in DMF (2 mL), followed by addition of N,N-Diisopropylethylamine (10.8 μL, 0.06 mmol). A solution of well dispersive **TiO_2-APTEs** (67 mg) in DMF (10 mL) was added and the reaction mixture was stirred overnight. Then, the reaction mixture was centrifuged at 10,000 g for 10 min. The centrifugate was washed with 10 mL DMF and water three times, respectively. Then the nanoparticles were dried in vacuo overnight.

TiO_2@Ru@siRNA: The **TiO_2@Ru-APTEs** nanoparticles were dispersed in pH 6.5 PBS buffer to a final concentration of 200 μg/mL. The HIF-1α-siRNA was added to the reaction until final concentration was 2 μM. The mixture was sired at 4 °C for 30 min. After then, the nanoparticles were centrifuged at 10,000 g for 10 min and washed with pH 6.5 PBS buffer three times. At last, the nanoparticles were dispersed with DEPC water.

See **supplementary information** for characterization details.

2.4. PDX model

The PDX model was established as described previously [41]. Tumor samples were collected at the Department of Head and Neck Surgery, Sun Yat-sen University Cancer Center. Prior informed consent was obtained from OSCC patient and the research was approved by the Medical Ethics of Committee of Hospital of Stomatology, Sun Yat-sen university (KQEC-2021-64-2). In brief, freshly resected tumors were intensively washed and cut into small pieces (diameter, 0.8–1.5 mm) in antibiotic containing DMEM. Then, the tumor pieces were implanted subcutaneously into the flanks of nude mice (P0 xenografts). The tumor size was measured using a vernier caliper when the inoculated tissue grew into the tumor. The tumor volume (mm^3) was calculated by the following formula: $V = a \times b^2/2$, where V represented the tumor volume, and a and b were the longest and shortest tumor diameters, respectively. When the tumor size reached 1500 mm^3, the tumors were dissected, processed and reinjected for expansion (P1 xenografts). This process was further repeated, and the animal study was performed with P6 xenografts. When the xenografts reached a mean size of 200 mm^3, the mice were randomized into 6 groups (5 mice per group) and treated as follows: (A) control (50 μL saline); (B) control (50 μL saline) + light; (C) **TiO_2@Ru** (50 μL, 20 mg/kg); (D) **TiO_2@Ru** (50 μL, 20 mg/kg) + light; (E) **TiO_2@Ru@siRNA** (50 μL, 20 mg/kg); (F) **TiO_2@Ru@siRNA** (50 μL, 20 mg/kg) + light. Mice were treated with **Ru** complexes twice at day 0 and day 7, and PDT was conducted with a 525 nm laser (15 mW cm^{-2}, 60 min) after intratumorally injection. Body weight and the subcutaneous tumor size were measured every other day. The mice were sacrificed 23 days after treatment. Tumor tissues were removed, weighed, fixed in 10% buffered formalin, and embedded in paraffin. And major organs including the heart, liver, spleen, lung, and kidney were removed and embedded in paraffin for histopathological assessment.

2.5. 4NQO-induced rat oral carcinogenesis model

The 4NQO-induced rat oral carcinogenesis model was established as described previously [42]. Male Sprague-Dawley (SD) rats (male, 4 weeks) were fed daily with 20 ppm 4NQO solution in their drinking water from week 0 to week 16. After the 16-week carcinogen treatment, the drinking water was switched to distilled water. The rats were divided into 4 groups (5 rats per group) and treated as follow: (A) control (150 μL saline); (B) control (150 μL saline) + light; (C) **TiO_2@Ru@siRNA** (150 μL, 20 mg/kg); (D) **TiO_2@Ru@siRNA** (150 μL, 20 mg/kg) + light. Rats were treated with **Ru** complexes twice at the start of week 17 and week 18, and PDT was conducted with a 525 nm laser (15 mW cm^{-2}, 60 min) after submucosal injection. At week 21, the rats were sacrificed and the tongues were dissected, and a longitudinal mid-lingual incision was made. Half of the specimens were fixed in 10% buffered formalin, embedded in paraffin and cut into 4 mm sections for hematoxylin and eosin (H&E) staining to confirm the pathological diagnosis. The other half of the specimens were stored at −80 °C.

All of the animal procedures were conducted in accordance with the Guidelines for the Care and Use of Laboratory Animals and were approved by the Institutional Animal Care and Use Committee at Sun Yat-sen University.

See **supplementary information** for the other experimental methods.

3. Results and discussion

3.1. Synthesis and characterization of TiO_2@Ru@siRNA

The **Ru** complex (**Ru**) was synthesized by the microwave reaction of the precursor $[Ru(dimbpc)_2]Cl_2$ with ligand **TTIP** (Scheme S1). The crude product (**Rua**) was hydrolyzed in NaOH to obtain the target product **Ru**. **Ru** was characterized by ESI-MS, ^1H NMR and ^{13}C NMR (Figure S2–S4).

The p25 **TiO_2** nanoparticles were embellished by APTEs, which endowed **TiO_2** with a positive potential (Scheme S2). **Ru** was coupled onto **TiO_2-APTEs** NPs to obtain **TiO_2@Ru** through amidation, and the maximum loading capacity was calculated to be 0.315 mg/mg (**Ru**/**TiO_2-APTEs**; Figure S5). TEM image of **TiO_2@Ru** shows a well-defined cube shape with a diameter of about 40 nm (Fig. 1A).

After conjugation of **Ru**, the vibration peaks of 3004 nm ($\nu_{C\text{-}H}$), 1655 nm ($\nu_{C=O}$), 1437 nm ($\beta_{C\text{-}H}$) and 1314 nm ($\nu_{C\text{-}N}$) were detected in the infrared (IR) spectrum of **TiO_2@Ru**, indicating that **Ru** has been successfully loaded on **TiO_2** (Fig. 1B). The UV–Vis spectrum of **TiO_2@Ru** shows **Ru** modification enhances the visible light absorption of the **TiO_2** NPs (Figure S6). The diameter measured by dynamic light scattering (DLS, Fig. 1C) is about 82 nm, which is larger than that measured by TEM, as DLS gives a hydrodynamic size that corresponds to the core and the swollen corona of the micelles, while TEM often gives a size of the core for micelles in a dried state.

The zeta potentials of p25 **TiO_2** and **TiO_2-APTEs** are −7.41 ± 1.22 and +27.65 ± 2.46 mV, respectively (Fig. 1D). The zeta potential is decreased with the increase in the **Ru** loading. In order to preserve the positive surface charges of the **TiO_2@Ru** NPs for optimized loading of negatively charged siRNA, 80% of the maximum loading capacity was used as the optimum loading ratio (0.252 mg/mg; **Ru**/**TiO_2-APTEs**). Quantitative energy dispersive X-ray (EDX) analysis shows the presence of Ti, Ru, C, N, O and S elements in **TiO_2@Ru**, and the mass proportion of Ru element is 1.6% (Fig. 1E). The weight percentage of the **Ru** coating measured by energy dispersive X-ray spectrometer (EDS) is 18.0%, which is similar to the weight percentage (25.2%) calculated by loading capacity measured by UV absorption calculation (Figure S5).

TiO_2 NPs can degrade the H_2O producing •OH, we next studied the water splitting capability of **TiO_2@Ru** under visible light irradiation (525 nm, 15 mW cm^{-2}, 30 min) using methylene blue as the indicator (Fig. 1F). Besides, the generation of •OH upon visible light irradiation (525 nm, 15 mW cm^{-2}, 30 min) is also been confirmed by electron spin resonance (ESR) using 5,5-dimethylpyrroline N-oxide (DMPO) as the trap for •OH (Fig. 1G). Both results indicate that **TiO_2@Ru** can effectively generate •OH after irradiation with visible light. The significant decrease of the absorbance of 9,10-anthracenediyl-bis (methylene) dimalonic acid (ABDA, an $^1O_2$ indicator) in the presence of **TiO_2@Ru** after irradiation shows that **TiO_2@Ru** can also efficiently photosensitize O_2 to generate $^1O_2$. The $^1O_2$ yield for **TiO_2@Ru** is 0.38, which is higher than the $^1O_2$ yield of **Ru** (0.28) under the same conditions (Fig. 1H).

The phosphorescent lifetime of **Ru** is greatly shortened by loading onto **TiO_2** NPs, which indicates there exists energy transfer between **Ru** and **TiO_2** NPs (Figure S7). Therefore, we propose that due to the energy transfer between the antenna (**Ru**) and **TiO_2**, **TiO_2** can be excited by visible light. **Ru** transfers the energy to the CB of **TiO_2** for effective electron hole separation (Fig. 1I). On the one hand, the process facilities the energy transfer from **TiO_2** to O_2 for the generation of $^1O_2$. On the other hand, •OH can be produced from the reaction between **TiO_2** holes and H_2O. Moreover, the conjugated **Ru** molecules can also produce •OH and $^1O_2$ upon irradiation (Fig. 1G and H).

The siRNA of HIF-1α was loaded onto **TiO_2@Ru** through electrostatic interaction to afford **TiO_2@Ru@siRNA** NPs. Agarose gel electrophoresis shows that 2.0 μM siRNA can be successfully loaded onto **TiO_2@Ru** NPs (200 μg/mL) at pH 6.5 (Fig. 1J), and the Zeta potential of **TiO_2@Ru@siRNA** is +1.14 ± 0.37 mV (Fig. 1K). TEM image of **TiO_2@Ru@siRNA** shows a well-defined cube shape with a diameter of about 50 nm (Figure S8A), and the hydrodynamic diameter for **TiO_2@Ru@siRNA** is about 100 nm as measured by DLS (Figure S8B).

After being placed in FBS for 7 days, no precipitate is observed and no significant change in the size of **TiO_2@Ru@siRNA** can be detected, which proves that it has good biological stability (Figure S9).

Table 1
Cytotoxicity (IC_{50}, μg/mL)[a] of the NPs on different cell lines[b].

Conditions	HN6			HSC-6			DOK		
	Dark	Light	PI[c]	Dark	Light	PI[c]	Dark	Light	PI[c]
Normoxia (20% O_2)									
Ru	> 112	0.26 ± 0.01	> 431	> 112	0.29 ± 0.01	> 386	> 112	0.25 ± 0.01	> 448
TiO_2@Ru	> 500	0.31 ± 0.02	> 1613	> 500	0.64 ± 0.03	> 781	> 500	0.71 ± 0.06	> 704
TiO_2@Ru@siRNA	> 500	0.18 ± 0.01	> 2778	> 500	0.49 ± 0.04	> 1020	> 500	0.59 ± 0.05	> 847
Hypoxia (1% O2)									
Ru	> 112	0.41 ± 0.01	> 273	> 112	0.40 ± 0.01	> 280	> 112	0.42 ± 0.01	> 267
TiO_2@Ru	> 500	0.47 ± 0.01	> 1064	> 500	1.16 ± 0.05	> 431	> 500	1.06 ± 0.04	> 472
TiO_2@Ru@siRNA	> 500	0.22 ± 0.01	> 2273	> 500	0.58 ± 0.04	> 862	> 500	0.61 ± 0.02	> 820

[a] The IC50 values are calculated based on the concentration of **Ru**.
[b] Cells were incubated with the tested compounds for 48 h and detected by MTT assay in the absence and presence of 525 nm light (15 mW cm^{-2}, 30 min).
[c] PI is the ratio of the IC50 value in the dark to that obtained upon light irradiation. Data are presented as the means ± standard deviations (SD).

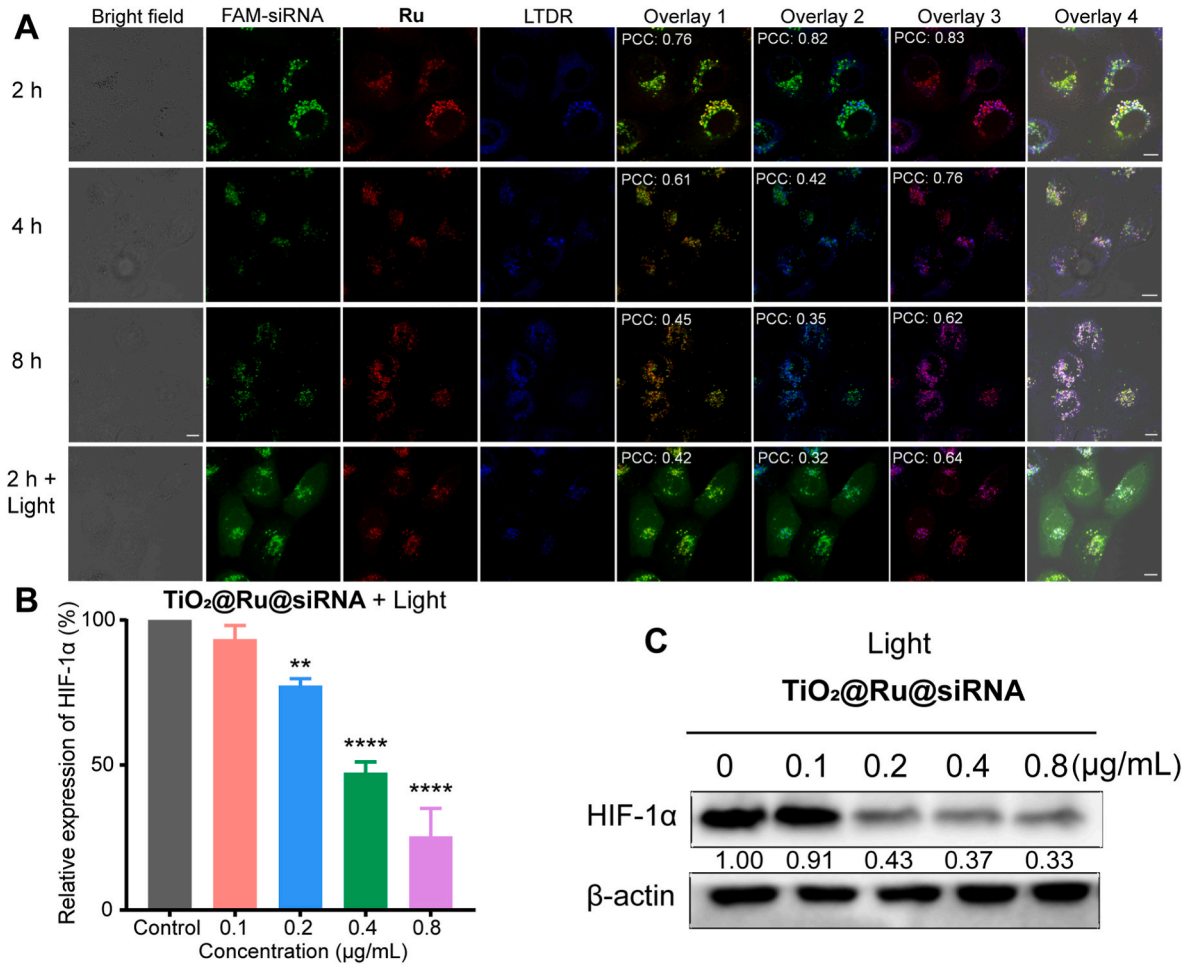

Fig. 2. Silence of HIF-1α by **TiO_2@Ru@siRNA**. (A) Time-dependent colocalization of **TiO_2@Ru@FAM-siRNA** with LTDR in HN6 cells. Cells were treated with **TiO_2@Ru@siRNA** (0.1 μg/mL) under normoxia and imaged by a confocal microscope at different time points in the absence and presence of light (525 nm, 15 mW cm^{-2}, 30 min). LTDR (200 nM) was added 15 min before imaging. Overlay 1: FAM-siRNA and **Ru**; Overlay 2: FAM-siRNA and LTDR; Overlay 3: **Ru** and LTDR; Overlay 4: FAM-siRNA, **Ru** and LTDR in bright filed. **Ru**: $\lambda_{ex} = 488$ nm; $\lambda_{em} = 630 \pm 20$ nm. FAM-siRNA: $\lambda_{ex} = 488$ nm; $\lambda_{em} = 510 \pm 20$ nm. LTDR: $\lambda_{ex} = 633$ nm; $\lambda_{em} = 720 \pm 20$ nm. Scale bars: 10 μm. (B, C) The expression of HIF-1α in HN6 cells treated with **TiO_2@Ru@siRNA** (0.1, 0.2, 0.4, 0.8 μg/mL, 24 h) in the presence of light (525 nm, 15 mW cm^{-2}, 30 min) was measured by RT-qPCR (B) and western blotting (C) under hypoxia. Quantitative analysis of western blotting was obtained to determine the relative intensity of HIF-1α. $^{**}p < 0.01$, $^{****}p < 0.0001$.

3.2. TiO_2@Ru@siRNA shows high phototoxicity under normoxia and hypoxia

The PDT activities of **Ru**, **TiO_2@Ru** and **TiO_2@Ru@siRNA** *in vitro* were evaluated on human tongue squamous cell carcinoma (HN6, HSC-6 and HSC-3) and dysplasia oral keratinocyte (DOK) cells by MTT assay (Table 1 and Table S1). Both under normoxic and hypoxic conditions, **Ru**, **TiO_2@Ru** and **TiO_2@Ru@siRNA** in the absence of light are nontoxic on all the cell lines tested. Generally, the phototoxicity follows the order: **TiO_2@Ru@siRNA** > **TiO_2@Ru** > **Ru**, and HN6 is the most sensitive cell line to the PDT treatment.

Under normoxic condition, the PI of **TiO_2@Ru@siRNA** in HN6 cells

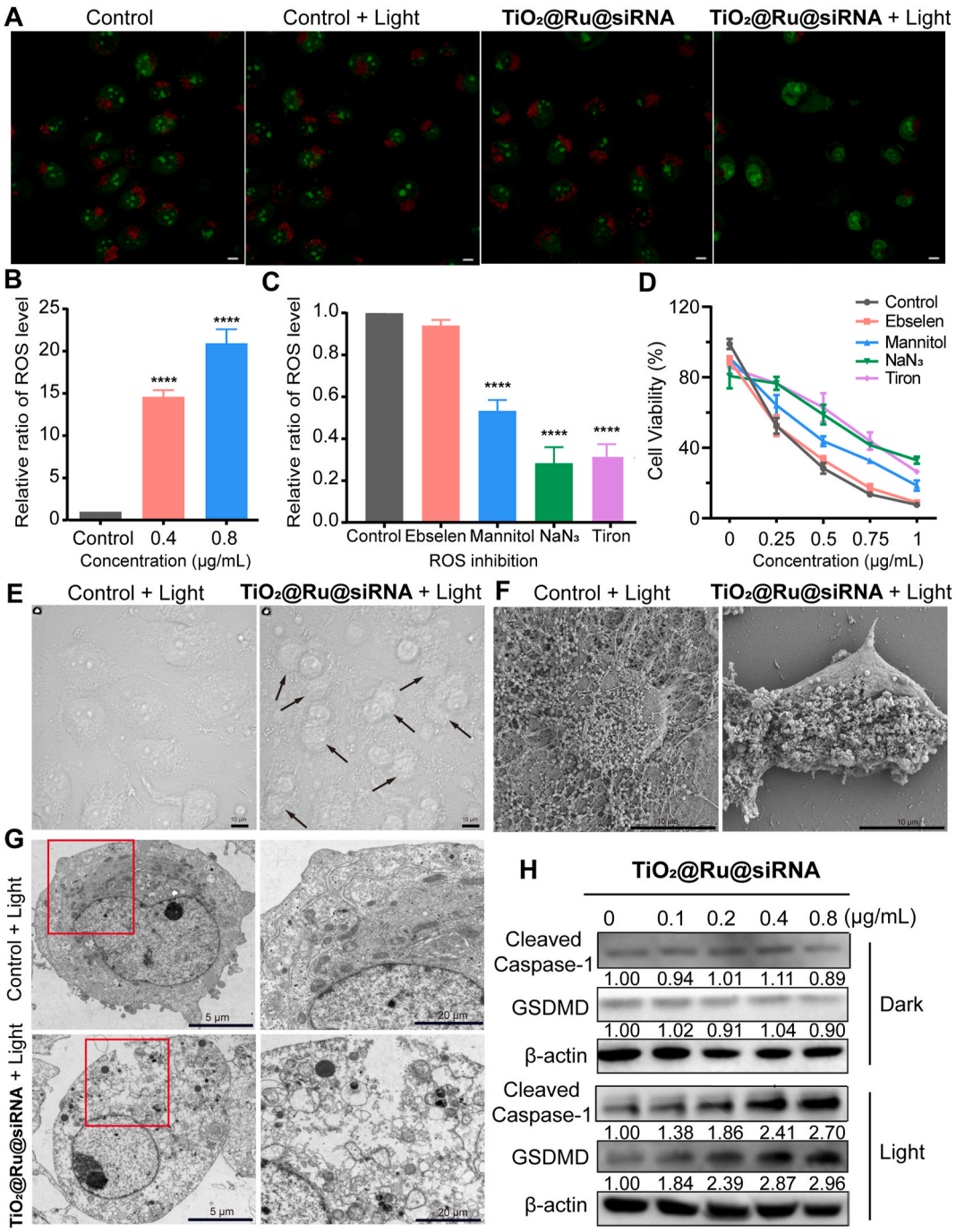

Fig. 3. **TiO_2@Ru@siRNA**-mediated PDT causes pyroptosis through lysosomal damage. (A) Impact of **TiO_2@Ru@siRNA** on lysosomal membrane permeability in HN6 cells measured by AO staining and confocal microscopy. The cells were treated with **TiO_2@Ru@siRNA** (0.8 μg/mL, 24 h) under hypoxia and then irradiated with a 525 nm laser (15 mW cm^{-2}, 30 min). λ_{ex} = 488 nm, λ_{em} = 525 ± 20 nm. Scale bars: 10 μm. (B) Intracellular ROS levels measured by DCFH-DA staining with flow cytometry. HN6 cells were treated with the **TiO_2@Ru@siRNA** (0.4, 0.8 μg/mL) for 24 h under hypoxia and irradiated with a 525 nm laser (15 mW cm^{-2}, 30 min) before incubated with DCFH-DA (10 μM, 15 min). λ_{ex} = 488 nm, λ_{em} = 525 ± 20 nm. (C) Impact of different ROS scavengers on the cellular ROS level. Cells were pre-incubated with the ROS scavengers for 2 h (Trion: 10 mM; NaN_3: 5 mM; D-mannitol: 50 mM; Ebselen: 50 μM). The cells were treated with **TiO_2@Ru@siRNA** (0.8 μg/mL, 24 h) under hypoxia and then irradiated with a 525 nm laser (15 mW cm^{-2}, 30 min). (D) The impact of ROS scavengers (Trion: 10 mM; NaN_3: 5 mM; D-mannitol: 50 mM; Ebselen: 50 μM) on the cell viability of **TiO_2@Ru@siRNA**. The cells were treated with **TiO_2@Ru@siRNA** (0.25, 0.5, 0.75, 1 μg/mL, 24 h) under hypoxia and then irradiated with a 525 nm laser (15 mW cm^{-2}, 30 min). (E) Bright field images by confocal microscope of HN6 cells treated with **TiO_2@Ru@siRNA** (0.8 μg/mL) for 24 h and then irradiated with a 525 nm laser (15 mW cm^{-2}, 30 min) under hypoxia. Scale bars: 10 μm. (F, G) The alternations in cell morphology upon PDT treatment by **TiO_2@Ru@siRNA** (0.8 μg/mL, 24 h) combined with a 525 nm laser (15 mW cm^{-2}, 30 min) detected by SEM (F) and TEM (G). Scale bars: 10 μm (SEM), 5 μm and 20 μm (TEM). (H) Western blotting of the impact of PDT by **TiO_2@Ru@siRNA** on the expression of GSDMD and cleaved caspase-1 in HN6 cells. Statistical analysis of western blotting to determine the relative intensity of GSDMD and cleaved caspase-1. The cells were treated with **TiO_2@Ru@siRNA** (24 h) at the indicated concentrations under hypoxia and then irradiated with a 525 nm laser (15 mW cm^{-2}, 30 min). ****$p < 0.0001$.

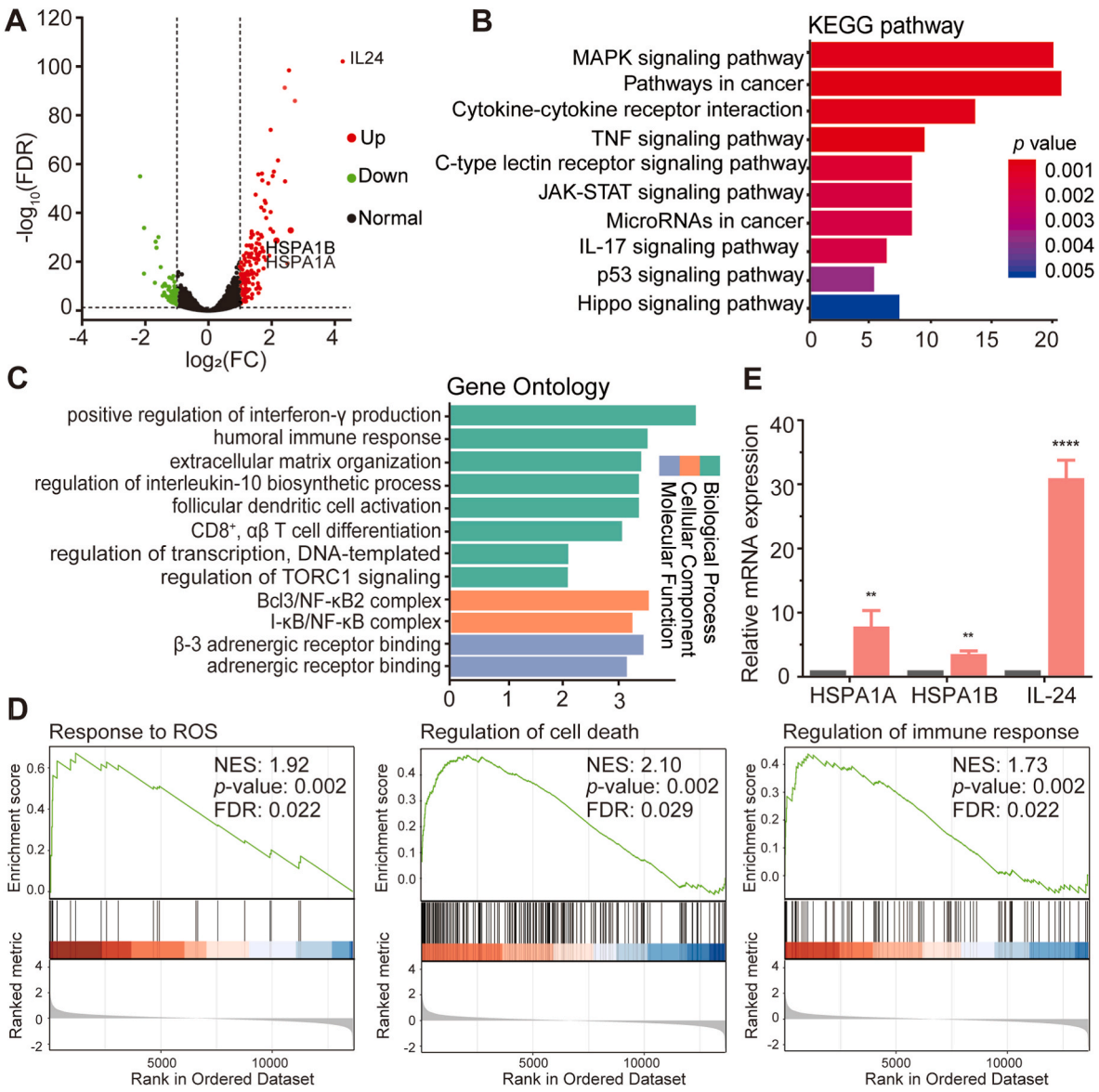

Fig. 4. The impact of **TiO_2@Ru@siRNA**-mediated PDT on transcriptome by RNA-seq. (A) Volcano plots showing the DEGs in HN6 cells treated with **TiO_2@Ru@siRNA**-mediated PDT. The cells were treated with **TiO_2@Ru@siRNA** (0.4 μg/mL, 24 h) under hypoxia + light (525 nm, 15 mW cm^{-2}, 30 min) and then incubated for another 4 h before mRNA extraction. (B) KEGG enrichment analysis of DEGs after **TiO_2@Ru@siRNA**-mediated PDT treatment. (C) GO term enrichment analysis of DEGs including biological process, cellular component, and molecular function was conducted to explain the enriched pathways and functions. (D) GSEA analysis of genes in different pathways. (E) RT-qPCR verification of the up-regulation of HSPA1A, HSPA1B and IL-24 mRNA in HN6 cells treated by **TiO_2@Ru@siRNA** (0.4 μg/mL, 24 h) under hypoxia with a 525 nm laser (15 mW cm^{-2}, 30 min). $^{**}p < 0.01$, $^{****}p < 0.0001$.

is about 5-fold higher than that of **Ru,** and difference in phototoxicity is found between **TiO_2@Ru** and **TiO_2@Ru@siRNA**. Similarly, phototoxicity of **Ru**, **TiO_2@Ru** and **TiO_2@Ru@siRNA** is well maintained under hypoxic condition, and a PI value higher than 2000 is observed for **TiO_2@Ru@siRNA** in HN6 cells. These results show that **TiO_2@Ru@siRNA** can overcome the hypoxic microenvironment of tumor, and the high PDT effects of **TiO_2@Ru@siRNA** are attributed to its capability to simultaneously act through both Type I and II pathways.

3.3. Silence of HIF-1α by TiO_2@Ru@siRNA

Considering that nanomaterials are usually retained in lysosomes/endosomes through endocytosis, firstly we studied the cellular localization of **TiO_2@Ru@siRNA** in OSCC cells using the commercial dye LTDR. To monitor the release of siRNA, HIF-1α siRNA in **TiO_2@Ru@siRNA** was labeled with carboxyfluorescein (FAM). After 2 h incubation, **TiO_2@Ru@FAM-siRNA** can be effectively absorbed by HN6 cells, and a high Pearson's correlation coefficient (PCC: 0.82) is observed for it with LTDR. Interestingly, with the extension of time, **Ru** can still form a good colocalization with LTDR, while the colocalization of FAM-siRNA with **Ru** and LTDR is gradually lost. The result indicates that siRNA successfully escapes from lysosomes/endosomes. Besides, the light irradiation can accelerate the release of FAM-siRNA from **TiO_2@Ru@siRNA** NPs, which may be attributed to the lysosomal damage by ROS generated by the NPs (Fig. 2A). Additionally, after 24 h incubation, most of the siRNA loaded on the nanoparticles has released to cytoplasm in the absence of light, which could protect the siRNA from the oxidization by the ROS produced in the following PDT process. Besides, the releasing of HIF-1α siRNA could also relieve the hypoxia status in cancer cells favoring for the development of photodynamic effect of the **TiO_2** nanoparticles (Figure S10).

As a consequence, both real-time quantitative polymerase chain

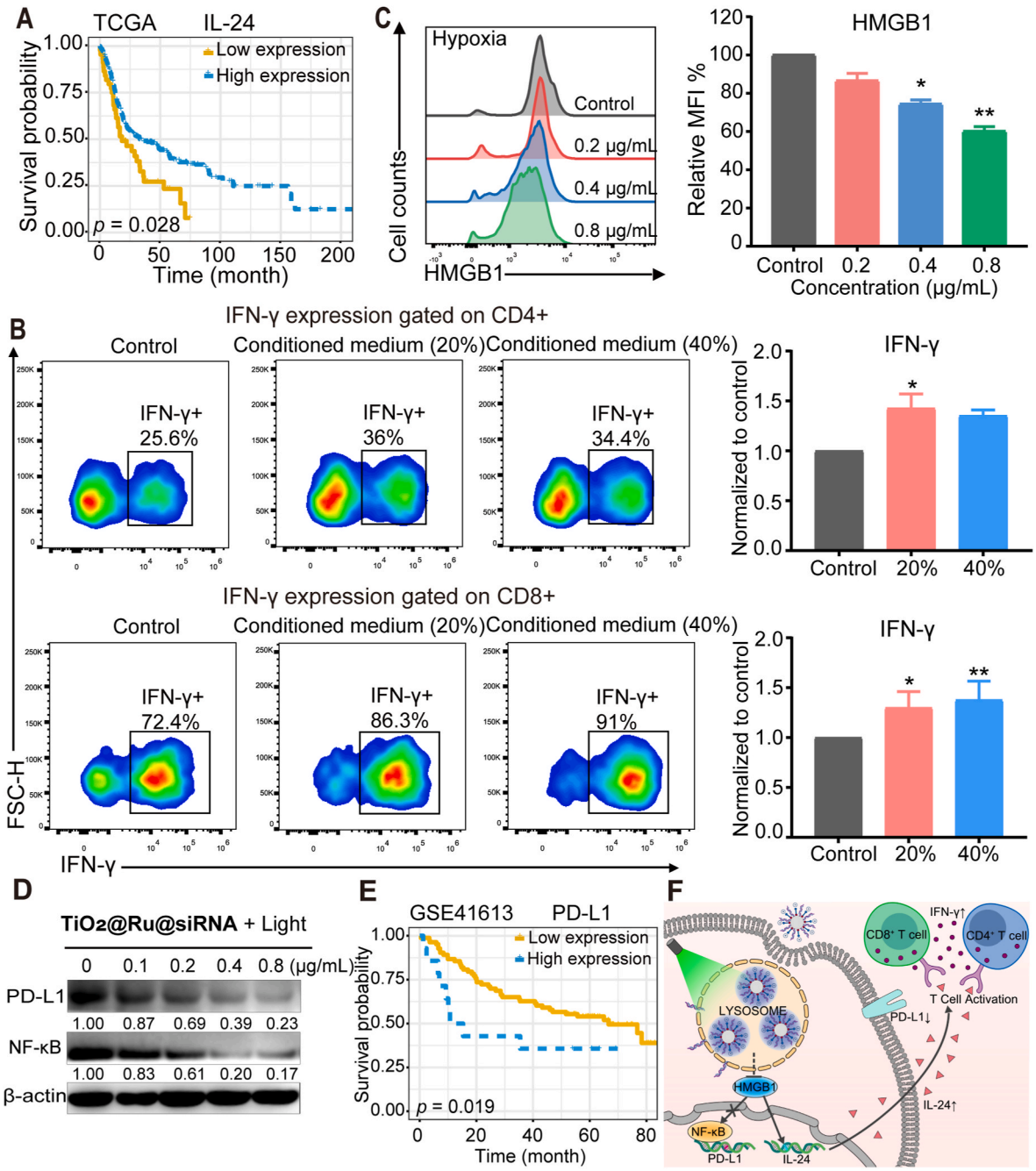

Fig. 5. **TiO_2@Ru@siRNA** enhances anticancer immunity. (A) Kaplan–Meier survival curve of overall survival based on head and neck squamous cell carcinoma patients with high- and low-expression of IL-24 in TCGA. (B) Representative flow cytometric analysis and relative expression of IFN-γ expression gated on $CD4^+$ T cells and $CD8^+$ T cells stimulated by conditioned medium. HN6 cells were treated with **TiO_2@Ru@siRNA** (0.4 μg/mL, 24 h) under hypoxia with a 525 nm laser irradiation (15 mW cm^{-2}, 30 min) and then incubated for another 24 h. The conditioned medium was collected and centrifuged at 500 g for 5 min to remove floating dead cells and debris. Peripheral blood mononuclear cells (PBMCs) were isolated from OSCC patients and stimulated by conditioned medium (20% and 40% in complete medium) for 48 h. (C) Flow cytometric analysis for the impact of PDT on the expression of HMGB1. HN6 cells were incubated with **TiO_2@Ru@siRNA** at the indicated concentrations (0.2, 0.4, 0.8 μg/mL) for 24 h and then irradiated with a 525 nm light array (15 mW cm^{-2}, 30 min) under hypoxia. (D) Impact of PDT on the expression of PD-L1 and NF-κB. Quantitative analysis of western blotting was obtained to determine the relative intensity of PD-L1 and NF-κB. HN6 cells were incubated with **TiO_2@Ru@siRNA** at the indicated concentrations (0.1, 0.2, 0.4, 0.8 μg/mL) for 24 h and then irradiated with a 525 nm light array (15 mW cm^{-2}, 30 min) under hypoxia. (E) Kaplan–Meier survival curve of overall survival based on OSCC patients with high- and low-expression of PD-L1 in GSE41613 dataset. (F) Schematic illustration of the mechanisms of cancer immunomodulatory effects by **TiO_2@Ru@siRNA**-mediated PDT. $^*p < 0.05$, $^{**}p < 0.01$.

reaction (RT-qPCR; Fig. 2B) and western blotting results suggest that HIF-1α is successfully knocked down under hypoxia in a concentration-dependent manner (Fig. 2C).

3.4. *TiO_2@Ru@siRNA-mediated PDT causes pyroptosis through lysosomal damage*

As **TiO_2@Ru@siRNA** localizes in lysosomes, we then evaluated the photo-damage of lysosomes by acridine orange (AO) staining upon PDT treatment. AO emits red fluorescence in acidic lysosomes and green

fluorescence in the cytoplasm and nuclei. The red dots representing acidic lysosomes are gradually disappeared upon **TiO_2@Ru@siRNA**-mediated PDT treatment, indicating the increase in the lysosomal membrane permeability (Fig. 3A).

The capability of **TiO_2@Ru@siRNA** to generate ROS upon light irradiation was detected using DCFH-DA staining, which can be oxidized to the highly emissive 2′,7′-dichlorofluorescein (DCF) by cellular ROS. In the presence of light, a concentration-dependent increase in DCF fluorescence is observed for **TiO_2@Ru** and **TiO_2@Ru@siRNA** under both normoxia and hypoxia. In the presence of light, **TiO_2@Ru@siRNA** (0.8 μg/mL) elevates the cellular ROS level to about 20-fold under both hypoxia and normoxia (Fig. 3B and Figure S11).

To confirm which kind of ROS played a major role in **TiO_2@Ru@siRNA**- and **TiO_2@Ru**-mediated PDT, the effects of different ROS scavengers (D-mannitol: •OH; Tiron: $\bullet O_2^-$; Sodium azide (NaN_3): $^1O_2$; Ebselen: $ONOO^-$) on the oxidative stress caused by the nanocomposites were investigated. Tiron, NaN_3 and mannitol effectively suppress the production of ROS by **TiO_2@Ru@siRNA** and **TiO_2@Ru** under both hypoxia and normoxia, while ebselen can only slightly reduce the ROS level. These results suggest that **TiO_2@Ru@siRNA** and **TiO_2@Ru** mainly produce $\bullet O_2^-$, $^1O_2$ and •OH to kill tumor cells upon PDT under hypoxia and normoxia (Fig. 3C and Figure S12). Moreover, Tiron, NaN_3 and mannitol markedly increase the viability of HN6 cells under hypoxia (Fig. 3D), while ebselen only slightly increases the viability of HN6 cells subjected to PDT treatment by **TiO_2@Ru@siRNA**, which further elaborates that $\bullet O_2^-$, $^1O_2$ and •OH account for the cell killing effect of PDT under hypoxia.

The alternations in cell morphology upon **TiO_2@Ru@siRNA** treatment in combination with light were detected by confocal microscopy, scanning electron microscopy (SEM) and TEM. Confocal images show that **TiO_2@Ru@siRNA**-mediated PDT causes swollen cells with large bubbles protruding from the plasma membrane under hypoxia and normoxia (Fig. 3E and Figure S13). SEM shows that control cells have clear outlines, long protuberances and tight cell connections, while cells treated with **TiO_2@Ru@siRNA** in combination with light display typical ultrastructural characteristics of pyroptosis including cell swelling, membrane rupture and reduction of numerous surface villi (Fig. 3F). TEM shows that cells treated with **TiO_2@Ru@siRNA** plus light appear complete loss of identifiable organelles and large disruption with numerous pores in the plasma membrane, in contrast to an intact plasma membrane and well-defined organelles from the control cells (Fig. 3G). Moreover, the key proteins of pyroptosis, gasdermin D (GSDMD) and cleaved caspase-1 [43], are upregulated upon PDT treatment with **TiO_2@Ru@siRNA** under both hypoxia and normoxia, which indicates **TiO2@Ru@siRNA**-mediated PDT induces caspase-1-dependent canonical pathway of pyroptosis (Fig. 3H and Figure S14). All these results show that **TiO_2@Ru@siRNA**-mediated PDT causes pyroptosis through lysosomal damage.

3.5. RNA-seq analysis

RNA-seq was further performed to investigate the impact of **TiO_2@Ru@siRNA**-mediated PDT on transcriptome. The correlation coefficients between every two individual samples from the same group are above 0.9 (Figure S15), indicating that the RNA-seq experiment is reproducible. The overall Q30% is above 92.33% (Table S2). More than 92.97% of readings are mapped to reference genes in all samples, and 84.53% of readings are located in exons (Table S3 and Figure S16). Compared with the control group, 210 significantly differentially expressed genes (DEGs; $|\text{Fold change}| \geq 2$; False discovery rate ≤ 0.05) are detected, of which 147 genes are significantly up-regulated and 63 genes down-regulated (Fig. 4A).

Kyoto Encyclopedia of Genes and Genomes (KEGG) enrichment analysis shows that DEGs caused by **TiO_2@Ru@siRNA**-mediated PDT are enriched in mitogen-activated protein kinase (MAPK) signaling pathway, pathway in cancer, cytokine-cytokine receptor interaction, janus kinase/signal transduction and activator of transcription (JAK-STAT) signaling pathway and apoptosis (Fig. 4B). These pathways are involved in cell proliferation, differentiation and apoptosis [44–46]. Especially, MAPK and JAK-STAT signaling pathways mediate lysosomal integrity [47,48].

Gene Ontology (GO) enrichment analysis shows that **TiO_2@Ru@siRNA**-mediated PDT mainly influences positive regulation of interferon-gamma (IFN-γ) production, regulation of interleukin-10 biosynthetic process, $CD8^+$ T cell differentiation, regulation of target of rapamycin complex 1 (TORC1) signaling and nuclear factor-kappa B (NF-κB) complex (Fig. 4C). These pathways are closely associated with cancer immunity [49–52]. Consistent with the fact that **TiO_2@Ru@siRNA** can photo-damage lysosomes, the significantly regulated TORC1 signaling is an important regulator of lysosomes, participating in lysosomal activation and regulating cell growth and metabolism [53].

As expected, gene set enrichment analysis (GSEA) shows that response to ROS, regulation to cell death and immune response related genes are upregulated after PDT treatment by **TiO_2@Ru@siRNA** (Fig. 4D). Several immune-related genes are found to be significantly upregulated upon PDT treatment by **TiO_2@Ru@siRNA** including interleukin-24 (IL-24) and heat shock protein family A (HSPA1A/HSPA1B) closely associated with cancer immune microenvironment (Fig. 4A).

Notably, IL-24, an immunomodulatory and tumor suppressor gene which is suppressed in many types of cancer [54], is significantly upregulated upon PDT treatment by **TiO_2@Ru@siRNA**. An increased expression of HSPA1A and HSPA1B, which can induce $CD8^+$ cytotoxic T lymphocyte and $CD4^+$ T helper cell responses [55], is also detected in **TiO_2@Ru@siRNA**-treated samples in the presence of light. The elevation in the transcription of HSPA1A, HSPA1B and IL-24 in samples with PDT is also verified by RT-qPCR (Fig. 4E).

3.6. TiO_2@Ru@siRNA enhances anticancer immunity

As RNA-seq shows that **TiO_2@Ru@siRNA**-mediated PDT can influence immune-related pathways, we then evaluate the effects of its capability to activate antitumor immunity. As previously indicated, IL-24, also known as melanoma differentiation-associated gene-7 (mda-7) [56], is upregulated upon PDT treatment. Kaplan–Meier analysis indicates that lower IL-24 expression predicts poorer prognosis for head and neck squamous cell carcinoma patients in the TCGA database (Fig. 5A).

As shown in Fig. 5B, conditioned medium using the supernatants of HN6 cells treated with **TiO_2@Ru@siRNA**-mediated PDT can stimulate the IFN-γ expression in both $CD4^+$ and $CD8^+$ T cells derived from the peripheral blood of OSCC patients compared with control group, which suggests that PDT treatment may enhance anti-tumor immunity efficiently in tumor microenvironment. To address whether IL-24 released by OSCC cells can affect antitumor immune response of OSCC as well, we examined the effects of exogenous IL-24 on cytokine expression. The results suggest that exogenous IL-24 significantly increases IFN-γ production in $CD4^+$ and $CD8^+$ T cells (Figure S17).

Moreover, the expression of high-mobility group box 1 protein (HMGB1) that can be induced by pyroptosis [57,58], exhibits a concentration-dependent decrease upon **TiO_2@Ru@siRNA**-mediated PDT under hypoxia (Fig. 5C). However, calreticulin (CRT) expression shows no significant change (Figure S18). These results suggest that **TiO_2@Ru@siRNA**-mediated PDT does not induce typical immunogenic cell death (ICD). The upregulation of IL-24 may be caused by the downregulation of HMGB1 induced by pyroptosis, as it has been reported that knockdown of HMGB1 can induce the upregulation of IL-24 [59].

The decreased expression of HIF-1α may downregulate PD-L1 [60], and the blockade of PD-L1 is effective in clinical cancer treatment [61]. Interestingly, **TiO_2@Ru@siRNA**-mediated PDT can decrease the expression of PD-L1. It has been reported that HMGB1-activated NF-κB

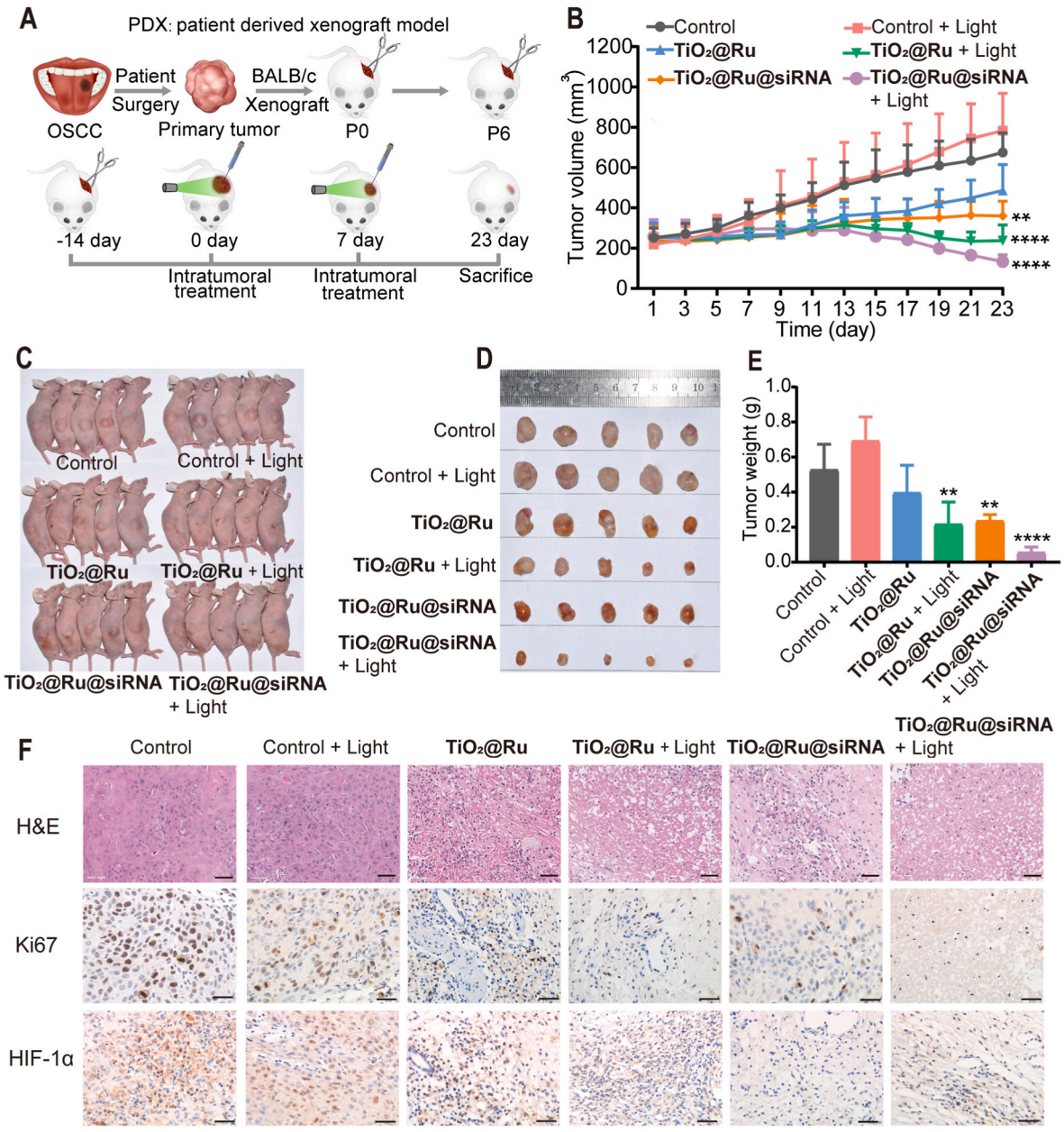

Fig. 6. **TiO_2@Ru@siRNA**-mediated PDT exhibits potent antitumor effects in PDX model. (A) Schematic illustration of the therapeutic protocol in PDX model. (B) Plots of the changes in tumor volumes during the treatment. (C, D) Representative images of tumor-bearing mice (C) and resected tumors (D) at the end of the treatment. (E) The tumor weight at the end of the treatment. (F) Representative H&E and IHC staining of Ki67 and HIF-1α in tumor sections from different groups. Scale bars: 50 μm $^{**}p < 0.01$, $^{****}p < 0.0001$.

contributes to cancer immune suppression [62]. Accordingly, the expression of NF-κB is also downregulated after PDT under hypoxia (Fig. 5D).

Meanwhile, Kaplan–Meier analysis indicates that significantly higher PD-L1 expression predicts poorer prognosis for OSCC patients in GSE41613 and GSE65858 datasets (Fig. 5E and Figure S1). These results indicate that the **TiO_2@Ru@siRNA**-mediated PDT can downregulate HMGB1 and NF-κB, which further inhibits PD-L1 to alleviate the cancer immunosuppression. Decreased expression of HMGB1 can also induce IL-24 upregulation to activate $CD4^+$ and $CD8^+$ T cells with IFN-γ secretion for enhanced anticancer immune responses. Therefore, the immunomodulatory effects induced by **TiO_2@Ru@siRNA**-mediated PDT may have a positive effect on cancer treatment (Fig. 5F).

3.7. *TiO_2@Ru@siRNA inhibits OSCC in PDX model*

PDX, in which tumor fragments surgically dissected from cancer patients are transplanted into immunodeficient mice, has emerged as a useful model for translational research to facilitate precision medicine [63]. PDX models reflect the diversity and heterogeneity of tumors, so the susceptibility of PDX to anticancer treatment is closely correlated with clinical data in patients [64]. Importantly, PDX can maintain the cellular and histopathological structure of their parental tumors. Therefore, PDX is a promising model in predicting the efficacy of conventional and novel anti-cancer therapies [65,66]. A PDX model was established in BALB/c mice (female, 4 weeks) to evaluate the antitumor effects of **TiO_2@Ru@siRNA** *in vivo* (Fig. 6A).

TiO_2@Ru@siRNA-medidated PDT shows a remarkable inhibition on tumor growth (Fig. 6B, C and D). At the end of the treatment, the

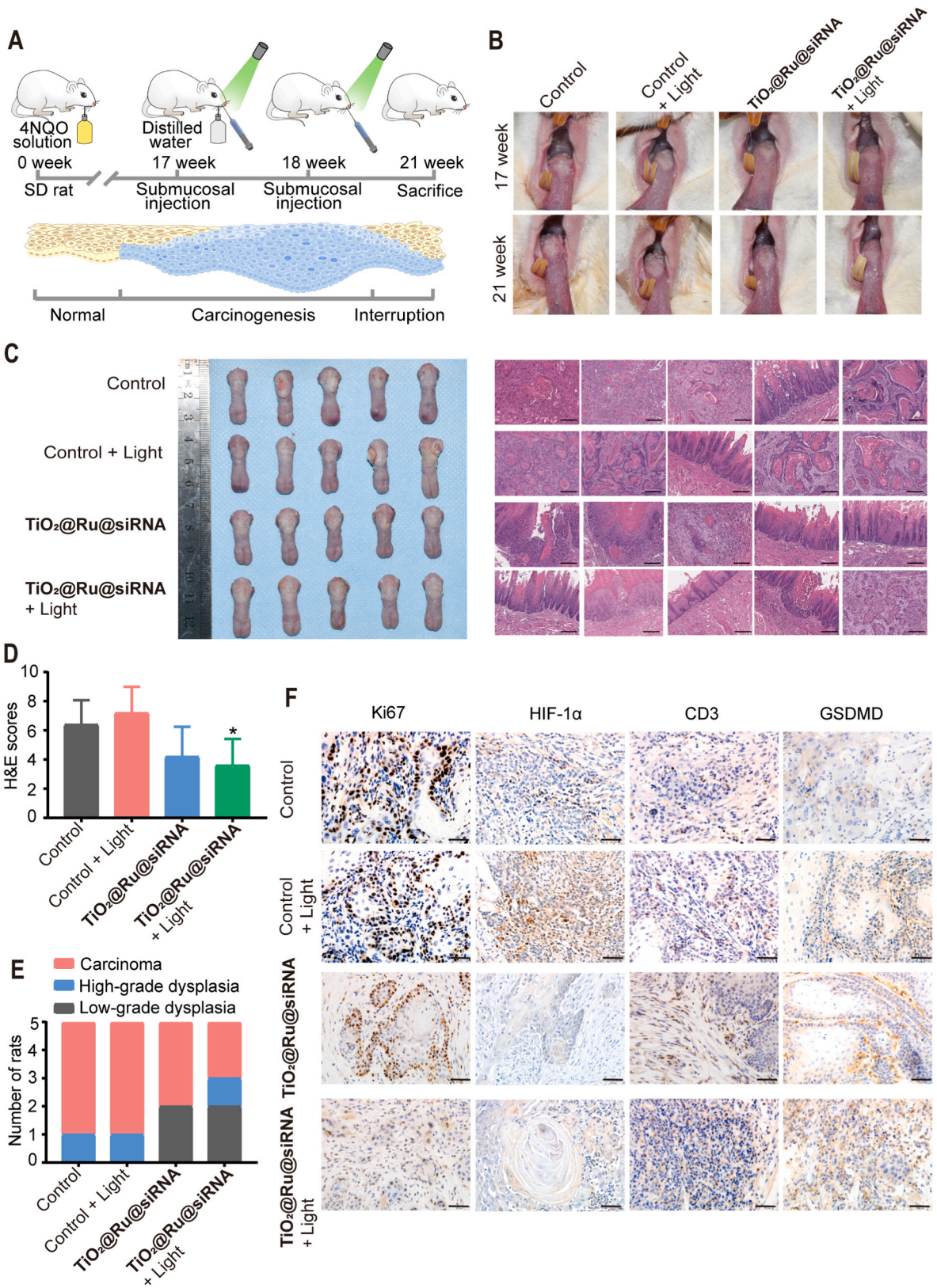

Fig. 7. **TiO_2@Ru@siRNA** inhibits carcinogenesis in 4NQO induced rat model. (A) Schematic overview of the 4NQO model experimental design. (B) Representative images of rat tongue lesions in the four groups at 17 week and 21 week. (C) Representative gross observation and H&E images of the rat tongues in different groups at endpoint. Scale bars: 200 μm. (D) H&E scores of the histopathologic diagnoses in the four groups. (E) Quantification of the histological ratio of low-grade dysplasia (normal and mild dysplasia), high-grade dysplasia (moderate and severe dysplasia), and carcinoma tissues in the four groups. (F) Representative IHC staining of Ki67, HIF-1α, CD3 and GSDMD. Scale bars: 50 μm $^*p < 0.05$.

tumor weight decreases by approximately 10-fold for **TiO_2@Ru@siRNA** group with PDT (Fig. 6E). H&E staining exhibits more necrotic foci in the **TiO_2@Ru@siRNA**-mediated PDT group. The nuclear antigen Ki67 is strongly associated with tumor cell proliferation and growth, and is widely estimated in the immunohistochemical (IHC) staining as a tumor proliferation marker. Consistently, IHC results show that the expression of Ki67 and HIF-1α is significantly decreased in **TiO_2@Ru@siRNA**-treated mice both in the absence and presence of light with the PDT group exerting a more profound effect (Fig. 6F).

Furthermore, no death or apparent decrease in body weights is found in all the groups (Figure S19), and H&E staining of the major organs reveals no noticeable organ damage, which indicates that **TiO_2@Ru@siRNA** NPs possess no systematic toxicity (Figure S20).

3.8. *TiO_2@Ru@siRNA inhibits carcinogenesis in 4NQO induced rat model*

The development of OSCC is a multistep and dynamic process, which includes developing stages of hyperplasia, dysplasia, carcinoma in situ and finally the invasive carcinoma [67]. 4NQO is a carcinogen known to induce DNA damage, leading to premalignant and malignant lesions in the oral cavity, which is similar to histological and molecular changes observed in human oral carcinogenesis [68]. Thus, 4NQO model provides an excellent opportunity to evaluate the capability of the anticancer treatment to intervene epithelial malignant transformation and tumor progression [69]. Therefore, after confirming the antitumor effect of **TiO_2@Ru@siRNA**-mediated PDT in PDX model, its potency to inhibit the carcinogenesis of 4NQO-induced rat model was further evaluated.

The schematic diagram of 4NQO rat model construction and therapeutic protocol is shown in Fig. 7A. After 4NQO exposure for 16 weeks, the lesions show granular hyperplasia, white flakes and spot plaques. At the end of the intervention, the lesions in the control group are accompanied by erosion, ulcer, and endogenous growth with unclear boundaries, while the lesions in **TiO_2@Ru@siRNA**-mediated PDT group still exhibit plaques (Fig. 7B). **TiO_2@Ru@siRNA**-treated mice in combination with light significantly interrupts the malignant transformation process. A histological comparison shows that the mean score of the **TiO_2@Ru@siRNA** group with PDT (HE score = 3.6) is significantly lower than that in the control group (HE score = 7.2; $p < 0.05$; Fig. 7C and D).

Furthermore, the proportion of samples with different malignant degree was calculated within each group. In the **TiO_2@Ru@siRNA** + PDT group, only 1 (20%) sample develops into carcinoma in situ and 1 (20%) sample develops into mild invasion carcinoma. While in control and control + PDT groups, 4 (80%) samples develop into invasion carcinoma (Fig. 7E and Table S4). IHC results show that the **TiO_2@Ru@siRNA** + PDT group significantly decreases the positive rates of Ki67 as well as HIF-1α and increases the expression of CD3 and GSDMD in tumors (Fig. 7F). Taken together, these results indicate that the **TiO_2@Ru@siRNA**-mediated PDT exhibits significant antitumor effects on OSCC *in vivo*. In particular, blocking the malignant transformation from dysplasia to cancer will be beneficial to clinical prevention for OSCC.

4. Conclusion

In all, we present a hypoxia-adaptive nanocomposite **TiO_2@Ru@siRNA** for photoimmunotherapy of OSCC. By causing lysosomal damage, **TiO_2@Ru@siRNA** effectively promotes the escape of HIF-1α siRNA for hypoxia improvement. **TiO_2@Ru@siRNA** NPs exert a very high PDT potency by elevating cellular ROS level through both O_2-dependent (Type II) and -independent (Type I) pathways to induce pyroptosis. Moreover, **TiO_2@Ru@siRNA**-mediated PDT effectively alleviates cancer immunosuppressive microenvironment and enhances the antitumor immune responses. Finally, **TiO_2@Ru@siRNA**-mediated PDT shows high potency in both the PDX and 4NQO-induced rat oral carcinogenesis models. In conclusion, we have constructed a hypoxia-adaptive photoimmunotherapeutic nanosystem for OSCC therapy, and its possibility of potential clinical transformation is still under exploration.

Credit author statement

Jia-Ying Zhou: Data curation, Methodology, Formal analysis, Investigation, Software, Writing – original draft. **Wen-Jin Wang**: Visualization, Methodology, Validation, Writing – original draft. **Chen-Yu Zhang**: Visualization, Methodology, Software, Validation, Writing – original draft. **Yu-Yi Ling**: Data curation, Methodology, Validation. **Xiao-Jing Hong**: Visualization, Resources, Validation. **Qiao Su**: Methodology, Validation. **Wu-Guo Li**: Methodology, Validation. **Zong-Wan Mao**: Methodology, Resources, Supervision. **Bin Cheng**: Methodology, Funding acquisition, Supervision. **Cai-Ping Tan**: Conceptualization, Formal analysis, Funding acquisition, Supervision, Writing – review & editing. **Tong Wu**: Conceptualization, Project administration, Funding acquisition, Supervision, Writing – review & editing.

Declaration of competing interest

The authors declare that they have no known competing financial interests or personal relationships that could have appeared to influence the work reported in this paper.

Data availability

Data will be made available on request.

Acknowledgements

This study was supported by the Science and Technology Planning Project of Guangzhou, China (grant number 202206080009), the Science and Technology Planning Project of Guangdong Province, China (grant number 2018B030317001), the National Natural Science Foundation of China (grant numbers 22022707, 22177142 and 21837006) and the Fundamental Research Funds for the Central Universities. J.Y. Zhou, W.J. Wang, C.Y. Zhang and Y.Y. Ling contributed equally to this work.

Appendix A. Supplementary data

Supplementary data to this article can be found online at https://doi.org/10.1016/j.biomaterials.2022.121757.

References

[1] B.W. Neville, T.A. Day, Oral cancer and precancerous lesions, CA A Cancer J. Clin. 52 (2002) 195–215.
[2] S.B. Chinn, J.N. Myers, Oral cavity carcinoma: current management, controversies, and future directions, J. Clin. Oncol. 33 (2015) 3269–3276.
[3] H.Y. Fan, Z.L. Zhu, W.L. Zhang, Y.J. Yin, Y.L. Tang, X.H. Liang, L. Zhang, Light stimulus responsive nanomedicine in the treatment of oral squamous cell carcinoma, Eur. J. Med. Chem. 199 (2020), 112394.
[4] R. Saini, N.V. Lee, K.Y. Liu, C.F. Poh, Prospects in the application of photodynamic therapy in oral cancer and premalignant lesions, Cancers 8 (2016).
[5] K. Konopka, T. Goslinski, Photodynamic therapy in dentistry, J. Dent. Res. 86 (2007) 694–707.
[6] W. Jerjes, T. Upile, Z. Hamdoon, C. Alexander Mosse, M. Morcos, C. Hopper, Photodynamic therapy outcome for T1/T2 N0 oral squamous cell carcinoma, Laser Surg. Med. 43 (2011) 463–469.
[7] M. Perez-Sayans, J.M. Suarez-Penaranda, G.D. Pilar, F. Barros-Angueira, J. M. Gandara-Rey, A. Garcia-Garcia, Hypoxia-inducible factors in OSCC, Cancer Lett. 313 (2011) 1–8.
[8] A.W. Eckert, C. Wickenhauser, P.C. Salins, M. Kappler, J. Bukur, B. Seliger, Clinical relevance of the tumor microenvironment and immune escape of oral squamous cell carcinoma, J. Transl. Med. 14 (2016) 85.
[9] X.C. Ding, L.L. Wang, X.D. Zhang, J.L. Xu, P.F. Li, H. Liang, X.B. Zhang, L. Xie, Z. H. Zhou, J. Yang, R.R. Weichselbaum, J.M. Yu, M. Hu, The relationship between

expression of PD-L1 and HIF-1alpha in glioma cells under hypoxia, J. Hematol. Oncol. 14 (2021) 92.
[10] S.K. Daniel, K.M. Sullivan, K.P. Labadie, V.G. Pillarisetty, Hypoxia as a barrier to immunotherapy in pancreatic adenocarcinoma, Clin. Transl. Med. 8 (2019) 10.
[11] R. Guo, Y. Li, Z. Wang, H. Bai, J. Duan, S. Wang, L. Wang, J. Wang, Hypoxia-inducible factor-1alpha and nuclear factor-kappaB play important roles in regulating programmed cell death ligand 1 expression by epidermal growth factor receptor mutants in non-small-cell lung cancer cells, Cancer Sci. 110 (2019) 1665–1675.
[12] Y. Wan, L.H. Fu, C. Li, J. Lin, P. Huang, Conquering the hypoxia limitation for photodynamic therapy, Adv. Mater. 33 (2021), e2103978.
[13] X. Li, N. Kwon, T. Guo, Z. Liu, J. Yoon, Innovative strategies for hypoxic-tumor photodynamic therapy, Angew. Chem., Int. Ed. Engl. 57 (2018) 11522–11531.
[14] M. Ovais, S. Mukherjee, A. Pramanik, D. Das, A. Mukherjee, A. Raza, C. Chen, Designing stimuli-responsive upconversion nanoparticles that exploit the tumor microenvironment, Adv. Mater. 32 (2020), e2000055.
[15] J.N. Liu, W. Bu, J. Shi, Chemical design and synthesis of functionalized probes for imaging and treating tumor hypoxia, Chem. Rev. 117 (2017) 6160–6224.
[16] A. Sharma, J.F. Arambula, S. Koo, R. Kumar, H. Singh, J.L. Sessler, J.S. Kim, Hypoxia-targeted drug delivery, Chem. Soc. Rev. 48 (2019) 771–813.
[17] O. Thews, P. Vaupel, Spatial oxygenation profiles in tumors during normo- and hyperbaric hyperoxia, Strahlenther. Onkol. 191 (2015) 875–882.
[18] M. Gao, C. Liang, X. Song, Q. Chen, Q. Jin, C. Wang, Z. Liu, Erythrocyte-membrane-enveloped perfluorocarbon as nanoscale Artificial red blood cells to relieve tumor hypoxia and enhance cancer radiotherapy, Adv. Mater. 29 (2017).
[19] Z. Shen, J. Xia, Q. Ma, W. Zhu, Z. Gao, S. Han, Y. Liang, J. Cao, Y. Sun, Tumor microenvironment-triggered nanosystems as dual-relief tumor hypoxia immunomodulators for enhanced phototherapy, Theranostics 10 (2020) 9132–9152.
[20] G. Lan, K. Ni, S.S. Veroneau, X. Feng, G.T. Nash, T. Luo, Z. Xu, W. Lin, Titanium-based nanoscale metal-organic framework for type I photodynamic therapy, J. Am. Chem. Soc. 141 (2019) 4204–4208.
[21] Y. Wang, Y. Li, Z. Zhang, L. Wang, D. Wang, B.Z. Tang, Triple-jump photodynamic theranostics: MnO2 combined upconversion nanoplatforms involving a type-I photosensitizer with aggregation-induced emission characteristics for potent cancer treatment, Adv. Mater. 33 (2021), e2103748.
[22] Y.Y. Zhao, L. Zhang, Z. Chen, B.Y. Zheng, M. Ke, X. Li, J.D. Huang, Nanostructured phthalocyanine assemblies with efficient synergistic effect of type I photoreaction and photothermal action to overcome tumor hypoxia in photodynamic therapy, J. Am. Chem. Soc. 143 (2021) 13980–13989.
[23] L. Li, C. Shao, T. Liu, Z. Chao, H. Chen, F. Xiao, H. He, Z. Wei, Y. Zhu, H. Wang, X. Zhang, Y. Wen, B. Yang, F. He, L. Tian, An NIR-II-emissive photosensitizer for hypoxia-tolerant photodynamic theranostics, Adv. Mater. 32 (2020), e2003471.
[24] H. Yuan, Z. Han, Y. Chen, F. Qi, H. Fang, Z. Guo, S. Zhang, W. He, Ferroptosis photoinduced by new cyclometalated iridium(III) complexes and its synergism with apoptosis in tumor cell inhibition, Angew. Chem., Int. Ed. Engl. 60 (2021) 8174–8181.
[25] S.A. McFarland, A. Mandel, R. Dumoulin-White, G. Gasser, Metal-based photosensitizers for photodynamic therapy: the future of multimodal oncology? Curr. Opin. Chem. Biol. 56 (2020) 23–27.
[26] O. Mazor, A. Brandis, V. Plaks, E. Neumark, V. Rosenbach-Belkin, Y. Salomon, A. Scherz, WST11, a novel water-soluble bacteriochlorophyll derivative; cellular uptake, pharmacokinetics, biodistribution and vascular-targeted photodynamic activity using melanoma tumors as a model, Photochem. Photobiol. 81 (2005) 342–351.
[27] I. Ashur, R. Goldschmidt, I. Pinkas, Y. Salomon, G. Szewczyk, T. Sarna, A. Scherz, Photocatalytic generation of oxygen radicals by the water-soluble bacteriochlorophyll derivative WST11, noncovalently bound to serum albumin, J. Phys. Chem. A 113 (2009) 8027–8037.
[28] S. Monro, K.L. Colon, H. Yin, J. Roque 3rd, P. Konda, S. Gujar, R.P. Thummel, L. Lilge, C.G. Cameron, S.A. McFarland, Transition metal complexes and photodynamic therapy from a tumor-centered approach: challenges, opportunities, and highlights from the development of TLD1433, Chem. Rev. 119 (2019) 797–828.
[29] J. Karges, Clinical development of metal complexes as photosensitizers for photodynamic therapy of cancer, Angew. Chem., Int. Ed. Engl. 61 (2022), e202112236.
[30] A. Fujishima, K. Honda, Electrochemical photolysis of water at a semiconductor electrode, Nature 238 (1972) 37–38.
[31] T. Rajh, N.M. Dimitrijevic, M. Bissonnette, T. Koritarov, V. Konda, Titanium dioxide in the service of the biomedical revolution, Chem. Rev. 114 (2014) 10177–10216.
[32] F.U. Rehman, C. Zhao, H. Jiang, X. Wang, Biomedical applications of nano-titania in theranostics and photodynamic therapy, Biomater. Sci. 4 (2016) 40–54.
[33] R. Cai, Y. Kubota, T. Shuin, H. Sakai, K. Hashimoto, A. Fujishima, Induction of cytotoxicity by photoexcited TiO2 particles, Cancer Res. 52 (1992) 2346–2348.
[34] S.S. Lucky, N.M. Idris, K. Huang, J. Kim, Z. Li, P.S. Thong, R. Xu, K.C. Soo, Y. Zhang, In vivo biocompatibility, biodistribution and therapeutic efficiency of titania coated upconversion nanoparticles for photodynamic therapy of solid oral cancers, Theranostics 6 (2016) 1844–1865.
[35] R.C. Gilson, K.C.L. Black, D.D. Lane, S. Achilefu, Hybrid TiO2 -ruthenium nano-photosensitizer synergistically produces reactive oxygen species in both hypoxic and normoxic conditions, Angew. Chem., Int. Ed. Engl. 56 (2017) 10717–10720.
[36] Z. Hou, Y. Zhang, K. Deng, Y. Chen, X. Li, X. Deng, Z. Cheng, H. Lian, C. Li, J. Lin, UV-emitting upconversion-based TiO2 photosensitizing nanoplatform: near-infrared light mediated in vivo photodynamic therapy via mitochondria-involved apoptosis pathway, ACS Nano 9 (2015) 2584–2599.
[37] S.S. Lucky, N. Muhammad Idris, Z. Li, K. Huang, K.C. Soo, Y. Zhang, Titania coated upconversion nanoparticles for near-infrared light triggered photodynamic therapy, ACS Nano 9 (2015) 191–205.
[38] M. Toyama, K. Inoue, S. Iwamatsu, N. Nagao, Syntheses and crystal structures of mono(2,2 '-bipyridine)dichlorobis(dimethyl sulfoxide-S)ruthenium(II) complexes, [RuCl2(bpy)(dmso-S)2], Bull. Chem. Soc. Jpn. 79 (2006) 1525–1534.
[39] Y. Arenas, S. Monro, G. Shi, A. Mandel, S. McFarland, L. Lilge, Photodynamic inactivation of Staphylococcus aureus and methicillin-resistant Staphylococcus aureus with Ru(II)-based type I/type II photosensitizers, Photodiagnosis Photodyn. Ther. 10 (2013) 615–625.
[40] L. Ye, R. Pelton, M.A. Brook, Biotinylation of TiO(2) nanoparticles and their conjugation with streptavidin, Langmuir 23 (2007) 5630–5637.
[41] Q. Hu, J. Peng, L. Jiang, W. Li, Q. Su, J. Zhang, H. Li, M. Song, B. Cheng, J. Xia, T. Wu, Metformin as a senostatic drug enhances the anticancer efficacy of CDK4/6 inhibitor in head and neck squamous cell carcinoma, Cell Death Dis. 11 (2020) 925.
[42] Y. Hong, L. Yang, C. Li, H. Xia, N.L. Rhodus, B. Cheng, Frequent mutation of p16 (CDKN2A) exon 1 during rat tongue carcinogenesis induced by 4-nitroquinoline-1-oxide, Mol. Carcinog. 46 (2007) 85–90.
[43] R. Loveless, R. Bloomquist, Y. Teng, Pyroptosis at the forefront of anticancer immunity, J. Exp. Clin. Cancer Res. 40 (2021) 264.
[44] E.F. Wagner, A.R. Nebreda, Signal integration by JNK and p38 MAPK pathways in cancer development, Nat. Rev. Cancer 9 (2009) 537–549.
[45] J. Lv, Y. Zhu, A. Ji, Q. Zhang, G. Liao, Mining TCGA database for tumor mutation burden and their clinical significance in bladder cancer, Biosci. Rep. 40 (2020).
[46] Y. Verhoeven, S. Tilborghs, J. Jacobs, J. De Waele, D. Quatannens, C. Deben, H. Prenen, P. Pauwels, X.B. Trinh, A. Wouters, E.L.J. Smits, F. Lardon, P.A. van Dam, The potential and controversy of targeting STAT family members in cancer, Semin. Cancer Biol. 60 (2020) 41–56.
[47] K.P. Hopfner, V. Hornung, Molecular mechanisms and cellular functions of cGAS-STING signalling, Nat. Rev. Mol. Cell Biol. 21 (2020) 501–521.
[48] D. Chmiest, N. Sharma, N. Zanin, C. Viaris de Lesegno, M. Shafaq-Zadah, V. Sibut, F. Dingli, P. Hupe, S. Wilmes, J. Piehler, D. Loew, L. Johannes, G. Schreiber, C. Lamaze, Spatiotemporal control of interferon-induced JAK/STAT signalling and gene transcription by the retromer complex, Nat. Commun. 7 (2016), 13476.
[49] L.B. Ivashkiv, IFNgamma: signalling, epigenetics and roles in immunity, metabolism, disease and cancer immunotherapy, Nat. Rev. Immunol. 18 (2018) 545–558.
[50] M. Reina-Campos, N.E. Scharping, A.W. Goldrath, CD8(+) T cell metabolism in infection and cancer, Nat. Rev. Immunol. 21 (2021) 718–738.
[51] L.C. Kim, R.S. Cook, J. Chen, mTORC1 and mTORC2 in cancer and the tumor microenvironment, Oncogene 36 (2017) 2191–2201.
[52] K. Taniguchi, M. Karin, NF-kappaB, inflammation, immunity and cancer: coming of age, Nat. Rev. Immunol. 18 (2018) 309–324.
[53] P. Jouandin, Z. Marelja, Y.H. Shih, A.A. Parkhitko, M. Dambowsky, J.M. Asara, I. Nemazanyy, C.C. Dibble, M. Simons, N. Perrimon, Lysosomal cystine mobilization shapes the response of TORC1 and tissue growth to fasting, Science 375 (2022), eabc4203.
[54] W. Ouyang, S. Rutz, N.K. Crellin, P.A. Valdez, S.G. Hymowitz, Regulation and functions of the IL-10 family of cytokines in inflammation and disease, Annu. Rev. Immunol. 29 (2011) 71–109.
[55] C. Figueiredo, M. Wittmann, D. Wang, R. Dressel, A. Seltsam, R. Blasczyk, B. Eiz-Vesper, Heat shock protein 70 (HSP70) induces cytotoxicity of T-helper cells, Blood 113 (2009) 3008–3016.
[56] S. Kreis, D. Philippidou, C. Margue, I. Behrmann, IL-24: a classic cytokine and/or a potential cure for cancer? J. Cell Mol. Med. 12 (2008) 2505–2510.
[57] G. Tan, C. Huang, J. Chen, F. Zhi, HMGB1 released from GSDME-mediated pyroptotic epithelial cells participates in the tumorigenesis of colitis-associated colorectal cancer through the ERK1/2 pathway, J. Hematol. Oncol. 13 (2020) 149.
[58] S. Wang, Y. Zhang, HMGB1 in inflammation and cancer, J. Hematol. Oncol. 13 (2020) 116.
[59] N. Senda, H. Yanai, S. Hibino, L. Li, Y. Mizushima, T. Miyagaki, M. Saeki, Y. Kishi, S. Hangai, J. Nishio, M. Sugaya, T. Taniguchi, S. Sato, HMGB1-mediated chromatin remodeling attenuates Il24 gene expression for the protection from allergic contact dermatitis, Proc. Natl. Acad. Sci. U.S.A. 118 (2021).
[60] T.C. Chen, C.T. Wu, C.P. Wang, W.L. Hsu, T.L. Yang, P.J. Lou, J.Y. Ko, Y.L. Chang, Associations among pretreatment tumor necrosis and the expression of HIF-1alpha and PD-L1 in advanced oral squamous cell carcinoma and the prognostic impact thereof, Oral Oncol. 51 (2015) 1004–1010.
[61] J.P. Foy, C. Bertolus, M.C. Michallet, S. Deneuve, R. Incitti, N. Bendriss-Vermare, M.A. Albaret, S. Ortiz-Cuaran, E. Thomas, A. Colombe, C. Py, N. Gadot, J. P. Michot, J. Fayette, A. Viari, B. Van den Eynde, P. Goudot, M. Devouassoux-Shisheboran, A. Puisieux, C. Caux, P. Zrounba, S. Lantuejoul, P. Saintigny, The immune microenvironment of HPV-negative oral squamous cell carcinoma from never-smokers and never-drinkers patients suggests higher clinical benefit of Ido1 and PD1/PD-L1 blockade, Ann. Oncol. 28 (2017) 1934–1941.
[62] X. Liu, B. Lu, J. Fu, X. Zhu, E. Song, Y. Song, Amorphous silica nanoparticles induce inflammation via activation of NLRP3 inflammasome and HMGB1/TLR4/MYD88/NF-kb signaling pathway in HUVEC cells, J. Hazard Mater. 404 (2021), 124050.
[63] M. Hidalgo, F. Amant, A.V. Biankin, E. Budinska, A.T. Byrne, C. Caldas, R. B. Clarke, S. de Jong, J. Jonkers, G.M. Maelandsmo, S. Roman-Roman, J. Seoane, L. Trusolino, A. Villanueva, Patient-derived xenograft models: an emerging platform for translational cancer research, Cancer Discov. 4 (2014) 998–1013.

[64] G.J. Yoshida, Applications of patient-derived tumor xenograft models and tumor organoids, J. Hematol. Oncol. 13 (2020) 4.
[65] P. Tan, H. Cai, Q. Wei, X. Tang, Q. Zhang, M. Kopytynski, J. Yang, Y. Yi, H. Zhang, Q. Gong, Z. Gu, R. Chen, K. Luo, Enhanced chemo-photodynamic therapy of an enzyme-responsive prodrug in bladder cancer patient-derived xenograft models, Biomaterials 277 (2021), 121061.
[66] J. Huang, C. Zhuang, J. Chen, X. Chen, X. Li, T. Zhang, B. Wang, Q. Feng, X. Zheng, M. Gong, Q. Gong, K. Xiao, K. Luo, W. Li, Targeted drug/gene/photodynamic therapy via a stimuli-responsive dendritic-polymer-based nanococktail for treatment of EGFR-TKI-resistant non-small-cell lung cancer, Adv. Mater. 34 (2022), e2201516.
[67] A.C. Chi, T.A. Day, B.W. Neville, Oral cavity and oropharyngeal squamous cell carcinoma–an update, CA A Cancer J. Clin. 65 (2015) 401–421.
[68] D. Kanojia, M.M. Vaidya, 4-nitroquinoline-1-oxide induced experimental oral carcinogenesis, Oral Oncol. 42 (2006) 655–667.
[69] M. Vered, N. Yarom, D. Dayan, 4NQO oral carcinogenesis: animal models, molecular markers and future expectations, Oral Oncol. 41 (2005) 337–339.